Key Points:

- Large greigite particles (up to 75 µm) occur in multiple intensely bioturbated turbidite horizons offshore Sumatra
- Greigite formed under nonsteady state conditions modulated by successive organic matter-enriched turbidites and intensive bioturbation
- Greigite in bioturbated turbidites preserves primary (quasi-)syn-sedimentary magnetic records and is an important iron and sulfur sink

Correspondence to:

T. Yang and X. Zhao,
tyang@cugb.edu.cn;
xzhao@tongji.edu.cn

Author Contributions:

Conceptualization: Tao Yang, Mark J. Dekkers, Xixi Zhao
Funding acquisition: Tao Yang, Xixi Zhao, Katerina E. Petronotis
Investigation: Tao Yang, Mark J. Dekkers, Xixi Zhao, Katerina E. Petronotis, Yu-Min Chou
Methodology: Tao Yang, Mark J. Dekkers, Yu-Min Chou
Writing – original draft: Tao Yang

Greigite Formation Modulated by Turbidites and Bioturbation in Deep-Sea Sediments Offshore Sumatra

Tao Yang[1,2] , Mark J. Dekkers[2] , Xixi Zhao[3] , Katerina E. Petronotis[4] , and Yu-Min Chou[3]

[1]State Key Laboratory of Geological Processes and Mineral Resources, School of Geophysics and Information Technology, China University of Geosciences, Beijing, China, [2]Paleomagnetic Laboratory Fort Hoofddijk, Department of Earth Sciences, Utrecht University, Utrecht, The Netherlands, [3]Department of Ocean Science and Engineering, Southern University of Science and Technology, Shenzhen, China, [4]International Ocean Discovery Program, Texas A&M University, College Station, TX, USA

Abstract Authigenic greigite may form at any time within a sediment during diagenesis. Its formation pathway, timing of formation, and geological preservation potential are key to resolving the fidelity of (paleo-)magnetic signals in greigite-bearing sediments. In the cored sequence of the International Ocean Discovery Program Expedition 362 (Sumatra Subduction Margin), multiple organic-rich mudstone horizons have high magnetic susceptibilities. The high-susceptibility horizons occur immediately below the most bioturbated intervals at the top of muddy turbidite beds. Combined mineral magnetic, microscopic, and chemical analyses on both thin sections and magnetic mineral extracts of sediments from a typical interval (∼1,103.80–1,108.80 m below seafloor) reveal the presence of coarse-grained greigite aggregates (particles up to 50–75 µm in size). The greigite formed under nonsteady state conditions caused by the successive turbidites. Organic matter, iron (oxy)(hydr)oxides, Fe^{2+}, and sulfides and/or sulfate were enriched in these intensively bioturbated horizons. This facilitated greigite formation and preservation within a closed diagenetic system created by the ensuing turbidite pulse, where pyritization was arrested due to insufficient sulfate supply relative to Fe (oxy)(hydr)oxide. This may represent a novel greigite formation pathway under conditions modulated by turbidites and bioturbation. Paleomagnetic analyses indicate that the early diagenetic greigite preserves primary (quasi-)syn-sedimentary magnetic records. The extremely high greigite content (0.06–1.30 wt% with an average of 0.50 wt% estimated from their saturation magnetization) implies that the bioturbated turbiditic deposits are an important sink for iron and sulfur. Mineral magnetic methods, thus, may offer a window to better understand the marine Fe–S–C cycle.

Plain Language Summary Greigite (Fe_3S_4, a magnetic iron sulfide) may grow in the sediment column at any time during diagenesis. Its formation complicates interpretation of sedimentary magnetic records. A thorough understanding of greigite formation pathways is, thus, a prerequisite for paleomagnetic/environmental magnetic studies of greigite-bearing sediments. Natural greigite particles are often reported to be smaller than a few hundred nanometers in size. Here, we find large greigite concentrations with crystal sizes up to several tens of micrometers in multiple mudstone horizons in deep-sea sediments offshore Sumatra. These natural greigite crystals are the largest ever reported, and currently known greigite formation pathways cannot explain their size. Through detailed rock magnetic, microscopic, and chemical analyses, we propose that formation of these large greigite crystals is favored by successive organic-rich turbidites that have been intensively reworked by benthic fauna. We also demonstrate that these greigite-bearing sediments provide a reliable magnetic record for paleomagnetic studies. Our work may represent a new pathway for greigite formation and is important for studies of greigite-bearing sediments from similar settings. The greigite concentration appears to be extremely high. Thus, greigite formed by this pathway may be an overlooked iron–sulfur sink that should be considered when assessing the marine iron–sulfur–carbon cycle.

1. Introduction

Greigite (Fe_3S_4), the thiospinel of iron, is strongly ferrimagnetic. It can form as a precursor to pyrite (FeS_2) during sulfidic or methanic diagenesis in anoxic sedimentary environments (see review by Roberts et al. [2011]), or as magnetosome nanoparticles produced by magnetotactic bacteria in sulfidic aquatic environments (see review by Kopp and Kirschvink [2008]). The authigenic pathway involves two complex biogeochemical processes: that is, organoclastic sulfate reduction (OSR) or anaerobic oxidation of methane (AOM), as well as iron (oxy)(hydr)oxide

Writing – review & editing: Tao Yang, Mark J. Dekkers, Xixi Zhao, Katerina E. Petronotis, Yu-Min Chou

reduction (Roberts, 2015; Roberts et al., 2011). Via these reactions, the necessary reactants for greigite formation (i.e., dissolved iron and sulfide) are supplied. Greigite is considered to be metastable but has been reported to be generated and preserved in diverse environmental settings with ages ranging from the Ediacaran to the Holocene, although the greigite could be younger than its host sediment. Environments include organic-rich lacustrine and marine sediments, restricted anoxic basins, gas hydrate systems, and hydrothermal/cold seep environments (e.g., Badesab et al., 2020; Dewangan et al., 2013; Dong et al., 2013; Greve et al., 2021; Horng, 2018; Housen & Musgrave, 1996; Kars, Greve, & Zerbst, 2021; Kars, Köster, Henkel, et al., 2021; Kelder et al., 2018; Krs et al., 1990; Larrasoaña et al., 2007; Reynolds et al., 1994; Roberts et al., 1996; Sagnotti & Winkler, 1999; Snowball, 1991; Vasiliev et al., 2007, 2008).

Greigite can in principle form at any time (i.e., during early, late, or progressive diagenetic processes) when dissolved iron and sulfide required for its formation are available (Roberts, 2015 and references therein). Early greigite authigenesis, which is modulated by nonsteady state inputs of organic matter and iron-bearing minerals, is generally associated with OSR, AOM, or methane hydrate formation (e.g., Ebert et al., 2020; Jørgensen et al., 2004; Kars & Kodama, 2015; Kasten et al., 1998; Larrasoaña et al., 2007; J. Liu et al., 2004; Neretin et al., 2004). Late diagenetic reactions that cause greigite formation generally occur episodically in localized intervals (e.g., in permeable zones or faults) driven by incursions of sulfate- or sulfide-bearing fluids (e.g., Greve et al., 2021; Horng, 2018; Roberts & Weaver, 2005; Weaver et al., 2002). Hydrocarbon-rich fluids or clathrates also play an important role (e.g., Housen & Musgrave, 1996; Larrasoaña et al., 2007; Musgrave et al., 1995, 2019; Reynolds et al., 1994). For example, punctuated greigite diagenesis has been reported following the introduction of sulfate and methane-rich pore fluids in sediments from International Ocean Discovery Program (IODP) Site U1437, Izu-Bonin rear arc (Japan; Musgrave et al., 2019). Thermal maturation due to burial typically drives progressive diagenesis: the continual loss of fine-grained magnetite and gradual pyritization of greigite. These processes are argued to occur from the subsurface to depths corresponding to a burial temperature of ~60°C (e.g., Aubourg et al., 2012; Kars, Greve, & Zerbst, 2021; Kars, Köster, Henkel, et al., 2021; Kars et al., 2012, 2014; Musgrave et al., 2019).

Regardless of the greigite formation processes, detrital sedimentary iron (oxy)(hydr)oxides undergo partial or complete reductive dissolution. Greigite formation at the expense of iron oxides (especially magnetite) would, thus, lead to a partial (or even complete) overprinting of the primary depositional remanent magnetization in sediments, which will complicate or compromise interpretation of their magnetic recording (e.g., Florindo & Sagnotti, 1995; Horng et al., 1992, 1998; Jiang et al., 2001; Roberts & Turner, 1993; Roberts & Weaver, 2005; Robinson, 2001; Robinson & Sahota, 2000; Sagnotti et al., 2010). Knowledge of the mode and timing of greigite formation and its geological preservation potential are, therefore, key to resolving the fidelity of (paleo-)magnetic signals carried by greigite-bearing sediments, which is crucial for paleomagnetic and environmental magnetic studies (e.g., Aben et al., 2014; Y. Chen et al., 2021; Duan et al., 2020; Ebert et al., 2021; C.-F. Fu et al., 2015; Jiang et al., 2001; Just et al., 2019; Kelder et al., 2018; S.-Z. Liu et al., 2017; Nilsson et al., 2013; Roberts et al., 1996; Rowan et al., 2009; Vasiliev et al., 2007, 2008). It is also of interest for Fe–S–C geochemistry (e.g., Burton et al., 2011; Cutter & Kluckhohn, 1999; Johnston et al., 2014; Kao et al., 2004).

In marine sedimentary sequences, steady state conditions are often interrupted, for example, by organic matter input, sulfate reduction rate, and/or sedimentation rate variations (Larrasoaña et al., 2003; Roberts, 2015; Y. Wang et al., 2019). Under nonsteady state sedimentary conditions, limited sulfide concentrations or organic carbon supply relative to abundant reactive (ferrous) iron may arrest the pyritization process, favoring greigite production, and preservation (Kao et al., 2004; Roberts, 2015; Rowan et al., 2009). In the cored sequence of the IODP Expedition 362, Sumatra Subduction Margin, anomalously high magnetic susceptibilities are closely associated with the presence of greigite (see below for details). Greigite-rich intervals are observed in multiple horizons of structureless mudstone immediately underlying intensely bioturbated intervals at the top of muddy turbidite beds rich in plant material (McNeill, Dugan, Petronotis, et al., 2017). A primary example is seen in Core 362-U1480G-38R over the ~1,103.8–1,108.8 m below sea floor (mbsf) depth interval, which comprises mainly bioturbated black and gray clay and silty clay, where the highest magnetic susceptibility reaches ~15×10^{-3} SI (Figure 1). In this study, the mechanism of greigite formation and preservation under conditions modulated by turbidites and bioturbation was examined with mineral magnetic methods, to assess a previously underappreciated authigenic greigite source in marine sedimentary environments.
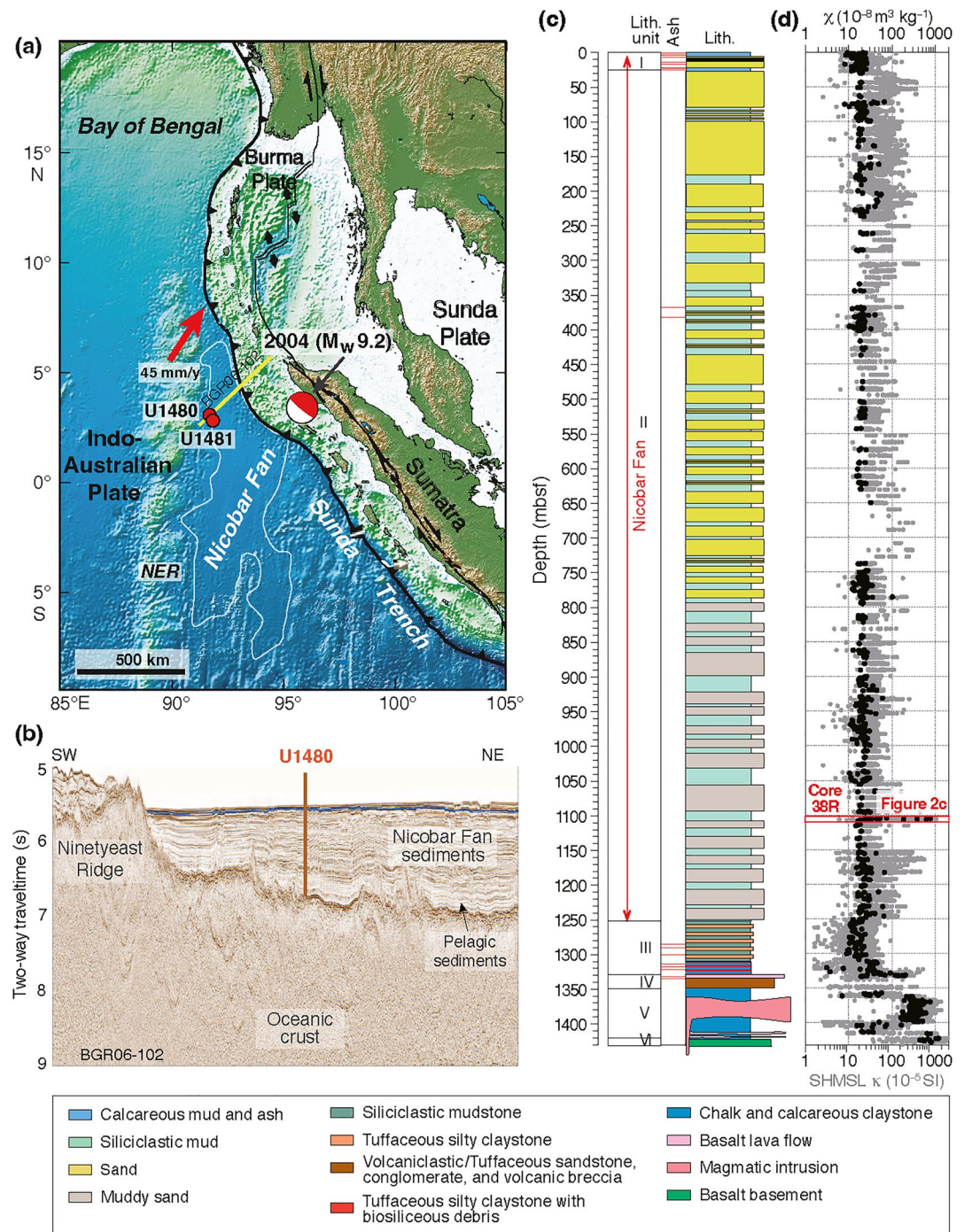
Figure 1. (a) Map of the north Sumatran subduction zone showing the location of drill sites U1480 and U1481 of International Ocean Discovery Program (IODP) Expedition 362 (red dots), and the epicenter of the 2004 Mw 9.2 Sumatra–Andaman earthquake (focal mechanism symbol). Red arrow with number is a convergence vector (mm/year). NER, Ninety East Ridge. (b) Interpreted seismic profile BGR06-102 (indicated in a) showing North Sumatran subduction input (i.e., Nicobar Fan sediments), with drill site U1480 (modified from McNeill, Dugan, Petronotis, et al. [2017]). (c) Lithostratigraphic units and subunits defined in Site U1480 (modified from McNeill, Dugan, Petronotis, et al. [2017]), mbsf = meters below sea floor. (d) Downhole mass-specific magnetic susceptibility (χ) measured on discrete samples and magnetic susceptibility (Section Half Multisensor Logger [SHMSL] κ) measured with the SHMSL instrument on archive-half sections for Site U1480. A close-up view of the ~1,103.8–1,108.8 mbsf interval (Core 38R) is shown in Figure 2c.

2. Geological Background and Samples

In the Sumatra–Andaman subduction channel, where the Indo-Australian plate subducts beneath the Burma–Sunda plate, a ~1,300-km-long rupture was produced along offshore northern Sumatra to the Andaman Islands by the 2004 Mw 9.2 earthquake (Figure 1a). In the Sumatra margin, the thickness of the incoming sediment wedge is up to ~4–5 km at the deformation front (McNeill, Dugan, Petronotis, et al., 2017). This is considerably thicker than in most other accretionary margins. The primary objective of IODP Expedition 362 is to establish the initial and evolving properties of the incoming sediments of the Indo-Australian oceanic plate and to assess their role in seismogenic process on Sumatra margin (McNeill, Dugan, Petronotis, et al., 2017).

During IODP Expedition 362, drilling and coring were conducted at two sites (Sites U1480 and U1481) located on the Indo-Australian Plate, east of Ninetyeast Ridge and ~250 km southwest of the subduction zone (Figures 1a and 1b). A detailed preliminary description of lithologic, physical, and geochemical properties is provided by McNeill, Dugan, Petronotis, et al. (2017). At Site U1480 (water depth of 4,148 m), a thin, distal trench wedge section, the Nicobar Fan succession, and a prefan pelagic succession were revealed by seismic imaging (Figure 1b; McNeill, Dugan, Petronotis, et al., 2017). At Site U1480, eight holes (U1480A–U1480H) of different penetration depths were drilled and cored from the seafloor to 1,431.63 mbsf (Figure 1c). The whole recovered section consists of a late Cretaceous to Pleistocene sedimentary succession, as well as the basaltic basement of ocean crust (McNeill, Dugan, Petronotis, et al., 2017). Based on major lithologic changes, six lithostratigraphic units (and subunits) are recognized (Figure 1c). Units I–IIIA (0–1,310.10 mbsf) are identified as the Nicobar Fan. Units IIIB to V (1,310.10–1,415.35 mbsf) represent prefan deposits, while Unit VI (1,415.35–1,431.63 mbsf) is basaltic crust of the Indian Plate (McNeill, Dugan, Petronotis, et al., 2017).

The Nicobar Fan is dominated by sandy and muddy turbidites (Pickering et al., 2020). Bioturbated black and gray clay characterize its lower portion (i.e., subunit IIC, 784.33–1,250.35 mbsf), along with silty clay and structure-less muddy sand with abundant plant debris (McNeill, Dugan, Petronotis, et al., 2017; Pickering et al., 2020). According to age models for Expedition 362 sites (Backman et al., 2019; McNeill, Dugan, Backman, et al., 2017; McNeill, Dugan, Petronotis, et al., 2017), the Nicobar Fan formed during the 15.3–1.7 Ma interval with fluctuating sediment accumulation rates: a prominent increase in sedimentation rate occurred at ~9.2 Ma (~1,250 mbsf, the boundary between Units IIIA and IIC): from 8 to 15 m/million years (m.y.) to ~220 m/m.y. The high sedimentation rate remained, but then decreased to 65–125 m/m.y. at 5.9 Ma (~520 mbsf) to increase again to 290 m/m.y. at ~2.4 Ma (~205 mbsf). The sedimentation rate subsequently dropped to 3–42 m/m.y. from ~1.7 Ma onward (~25 mbsf, boundary between Units I and II).

To quantify the bioturbation level, the ichnofabric index (Droser & Bottjer, 1986) was identified in cores with the help of visual charts (Heard et al., 2014). The bioturbation index (BI) represents the disturbed degree of primary sedimentary fabric (e.g., lamination) by biological activity and ranges from 1 for nonbioturbated to 6 for total homogenization (see McNeill, Dugan, Petronotis, et al. [2017] for details). Bioturbation is commonly low to moderate and tends to increase upward within turbidite beds, that is, the most bioturbated horizons (BI = 6) are generally located at the top of turbidite beds (Figures 2a, 2b, and 2g–2i).

For this study, 18 oriented discrete samples (~7 cm^3 volume) were taken from Core 362-U1480G-38R using Natsuhara-Giken plastic cubes. Excess sediment was also collected in plastic bags for shore-based mineral magnetic analyses. These samples are from different portions of turbidites with variable BI (Figure 2). This allows us to study the association of greigite formation with bioturbation and turbidites. All samples were stored in a freezer and isolated from air before undertaking the measurements described below.

3. Methods

3.1. Rock Magnetic Measurements

Shipboard magnetic susceptibility measurements were carried out with a Bartington Instruments MS2K surface sensor with a maximum sensitivity of 2×10^{-6} SI on the Section Half Multisensor Logger (SHMSL), operating at an alternating field (AF) of 100 μT and a 930 Hz frequency (see McNeill, Dugan, Petronotis, et al. [2017] for details). Measurements of low-field magnetic susceptibility (expressed on a mass-specific basis as χ) of discrete samples were carried out after the expedition with an MFK1-FA Multi-Function Kappabridge susceptometer (AGICO, Brno, Czech Republic) at the Paleomagnetic Laboratory of the State Key Laboratory of Marine
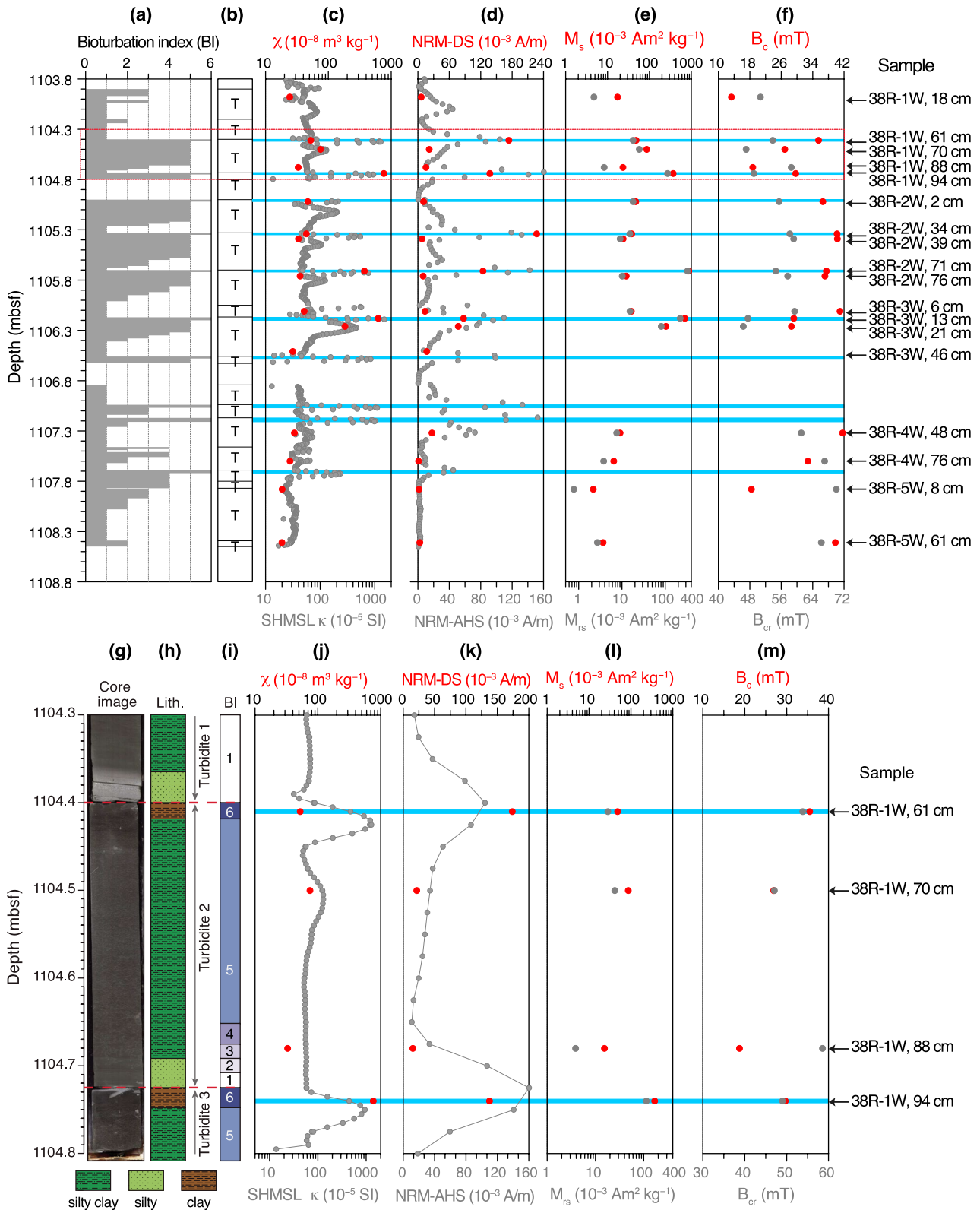
Figure 2.

Geology (PL-SKLMG), Tongji University (Shanghai, China). Detection limit and measurement accuracy of the instrument are 2×10^{-8} SI and 0.1%, respectively, at a 976 Hz frequency and in a 200 A/m (peak-to-peak) field.

Magnetic hysteresis measurements were made with a MicroMag™ Model 3900 vibrating sample magnetometer (VSM, Princeton Measurements Corporation, USA), at the Institute of Geophysics, China Earthquake Administration (Beijing, China). The maximum applied field was 1.0 T. Hysteresis parameters, that is, saturation magnetization (M_s), saturation remanence (M_{rs}), and coercive force (B_c) were determined from the hysteresis loops using the HystLab software (Paterson et al., 2018), and the remanent coercive force (B_{cr}) from the progressive back-field demagnetization of the isothermal remanent magnetization imparted at 1 T. First-order reversal curves (FORCs; Roberts et al., 2000) were measured for 13 selected samples to assess the magnetic domain state and to evaluate magnetostatic interactions. All FORC measurements were made with either the aforementioned VSM 3900 or a Lakeshore VSM 8604 (Lake Shore Cryotronics, Inc., USA) at the Institute of Geophysics and Geomatics, China University of Geosciences (CUG; Wuhan, China). We measured 120 curves for each FORC diagram with an averaging time of 0.1–0.2 s per data point and a ~2 mT field increment. The FORCinel package (Harrison & Feinberg, 2008) was used to process FORC diagrams (Pike et al., 1999).

A Quantum Design Inc. (San Diego, CA, USA) SQUID magnetometer (MPMS XL-7) with a sensitivity of 10^{-11} A m^2 was used for low-temperature (LT; down to 5 K) measurements. Fifteen selected samples with a mass of 120–150 mg were processed at the State Key Laboratory for Artificial Microstructure and Mesoscopic Physics, Peking University (Beijing, China). Each sample was subjected to three measurement cycles. (a) A LT saturation isothermal remanent magnetization (SIRM) was imparted in a 2.5 T after the sample was cooled from room temperature (300 K) to 5 K in zero field, which was then measured in a zero magnetic field during warming back to 300 K (termed ZFC for zero-field-cooled). (b) Next, the sample was cooled to 5 K again but now in a 2.5 T field, which was switched off at 5 K followed by measurement during warming to 300 K (termed FC for field-cooled). (c) Finally, a room temperature SIRM (RT-SIRM) was imparted in a 2.5 T field which was measured during cooling to 5 K and warming back to 300 K in a zero magnetic field. All the remanence measurements were made at intervals of 5 K.

Temperature-dependent magnetization was measured for 10 representative samples in air with a modified horizontal translation type Curie balance (noise level ~5×10^{-9} A m^2, Mullender et al., 1993) at the Paleomagnetic Laboratory Fort Hoofddijk, Utrecht University (the Netherlands). Stepwise thermomagnetic runs were carried out following the procedure described by Yang et al. (2018), with heating and cooling rates of 6 and 10°C/min, respectively.

3.2. Paleomagnetic Measurements

Split-core archive sections were measured onboard using a three-axis pass-through superconducting rock magnetometer (Model 760, 2G Enterprises, USA) equipped with an in-line automated AF demagnetizer. Successive AF demagnetization was performed in 4–6 steps for the natural remanent magnetization (NRM) to a maximum peak field of 25 mT using the in-line AF demagnetizer, with measurements made at 2.5 cm stratigraphic intervals (see Chapter "Expedition 362 methods" in McNeill, Dugan, Petronotis, et al. [2017] for details). In addition, thermal demagnetization of seven discrete samples was performed onboard using a thermal demagnetizer (ASC Model TD-48SC) at temperatures of 50°C, 75°C, 100°C, 150°C, 200°C, 250°C, 300°C, 325°C, 350°C, 400°C, and 450°C. Remanent magnetizations were measured on the JR-6A spinner magnetometer. The rest of the studied discrete samples were subjected to stepwise AF demagnetization after the expedition at PL-SKLMG, using a horizontal pass-through 2G Enterprises 755-4 K superconducting rock magnetometer (2G Enterprises, USA) equipped with an automatic sample handling system and in-line AF coils. Progressive static three-axis AF demagnetization was performed in 2.5 mT steps to a peak field of 10 mT, then in 5 mT steps to a peak field of 40 mT, then in 10 mT steps to a peak field of 60 mT, and finally a step at 80 mT. Principal component analysis (PCA; Kirschvink, 1980) was used to calculate the declination and inclination of the characteristic remanent

Figure 2. (a–f) Downhole bioturbation index (BI) and sediment magnetic parameters from the ~1,103.8–1,108.8 mbsf interval, Hole U1480G. The blue bars mark horizons with magnetic susceptibility spikes (MSS). An expanded view of the ~1,104.3–1,104.8 mbsf interval with a core image and lithology column is shown in (g)–(m). BI: 1 = no bioturbation, 2 = sparse, 3 = slight, 4 = moderate, 5 = heavy, and 6 = complete bioturbation; T, turbidite beds; NRM-DS, natural remanent magnetization (NRM) measured on discrete samples (red symbols); NRM-AHS, NRM measured on archive-half sections (gray symbols); χ, mass-specific magnetic susceptibility measured on discrete samples (red symbols); SHMSL κ, SHMSL magnetic susceptibility measured on archive-half sections (gray symbols); M_s, saturation magnetization (red symbols); M_{rs}, saturation remanence (gray symbols); B_c, coercive force (red symbols); and B_{cr}, remanent coercive force (gray symbols).

magnetization (ChRM) without anchoring to the origin of orthogonal projections, using the PuffinPlot software (Lurcock & Wilson, 2012) and www.paleomagnetism.org (Koymans et al., 2020).

3.3. Scanning Electron Microscopy/Energy Dispersive X-Ray Spectrometry Analyses and Electron Probe Microanalysis of Thin Sections

For scanning electron microscopy/energy dispersive X-ray spectrometry (SEM/EDS) and electron probe microanalysis (EPMA), bulk sediments were dried in an oven at ca. 40°C, then impregnated with epoxy resin under vacuum before being cut for polished thin sections. Slices with a thickness of ~1 mm were cut and polished to 80 μm thickness. Carbon-coated thin sections were analyzed for magnetic minerals with a Zeiss Sigma 300 field emission scanning electronic microscope (FE-SEM, Carl Zeiss, Germany) operated at 5–15 kV at the State Key Laboratory of Geological Processes and Mineral Resources, CUG (Wuhan, China). Backscattered and secondary electron imaging was carried out. Elemental compositions of individual mineral grains were determined by point analyses with the attached Oxford Instruments energy dispersive spectrometer. To confirm the standardless semiquantitative SEM/EDS determinations, the chemical compositions of magnetic minerals were also analyzed on polished thin sections using a JEOL JXA-8230 electron probe microanalyzer (JEOL, Japan) at the Center for Global Tectonics, School of Earth Sciences, CUG, Wuhan. The following operating conditions were used: 15 kV accelerating voltage, 20 nA cup current, and 2 μm beam diameter. Standards from Structure Probe, Inc. (SPI) were used: pyrite (Fe, S), magnetite (Fe), orthoclase (K), yttrium–aluminum–garnet (Al), albite (Si), pyrope (Mg), rhodonite (Mn), and rutile (Ti). Dwell times were 10 s on element peaks while those on background adjacent to peaks were 5 s. Raw X-ray intensities were corrected using a ZAF (atomic number, absorption, and fluorescence) algorithm (e.g., Goldstein et al., 2017).

3.4. X-Ray Diffraction Analysis and SEM Imaging of Magnetic Mineral Extracts

Magnetic particles were extracted from representative sediments with a different BI and magnetic susceptibility values for X-ray diffraction (XRD) analysis and microscopic observations. Approximately 200–500 mg subsamples were suspended in deionized water with sodium hexametaphosphate as dispersant in a beaker. Then, samples were ultrasonicated for 30 min to separate the magnetic minerals from the nonmagnetic fraction. A rare earth bar magnet was then used for isolating magnetic minerals from the suspension with gentle agitation; the procedure was repeated several times. The final extract was cleaned with deionized water and collected in centrifuge tubes. Magnetically extracted particles were dispersed in 10 mL ethanol.

For XRD analysis, magnetic extracts were transported to a glass slide using a pipette and dried in air. XRD analyses were then carried out using a Bruker D8 ADVANCE X-ray diffractometer (Bruker-AXS, Karlsruhe, Germany) with Cu-K$_\alpha$ X-ray radiation ($\lambda = 1.5406$ Å) in the 2θ range of 5°–70°, step size of 0.02°, and step count time of 0.5 s. After XRD analysis, a small portion of the magnetic extracts was transported to a double-sided carbon tape on sample holders for SEM imaging, which was conducted using a Zeiss Sigma SEM system (Carl Zeiss, Germany) coupled to an Oxford X-Max 50^N EDS detector (Oxford Instruments, UK). Backscattered electron images were obtained at a working distance of 8.5 mm and an accelerating voltage of 15 kV. Both XRD analysis and SEM imaging were carried out at the State Key Laboratory of Earthquake Dynamics, Institute of Geology, China Earthquake Administration (Beijing, China).

3.5. Total Organic Carbon and Total Nitrogen Measurements

Subsamples from representative sediments were dried at 50°C until constant weight, followed by grinding with an agate mortar and pestle. Approximately 10 mg of sediment was weighed into Ag capsules and decarbonated for total organic carbon (TOC) analysis with ~6%–8% sulfurous acid (H_2SO_3). Decarbonation was carried out following the procedure described by House (2019). Ag capsules with decarbonated sediment samples were sealed in Sn capsules to achieve efficient conversion of organic C to CO_2. Separate ~40 mg nondecarbonated portions of each sample were also sealed in Sn capsules for total nitrogen (TN) analysis.

TOC and TN analyses were made for 60 samples including samples from levels adjacent to the studied interval at the Stable Isotope Laboratory, University of California, Santa Cruz (CA, USA). Carbon and nitrogen amounts

were determined by Dumas combustion using a Carlo Erba 1108 elemental analyzer and estimated according to standards of known elemental composition with a precision better than 1%.

4. Results

4.1. XRD Patterns and SEM Imaging of Magnetic Mineral Extracts

XRD analysis of magnetic mineral extracts from six representative sediment samples with different magnetic susceptibility values provides clear diffraction patterns (Figure 3) for detailed mineral identification. Greigite, which is indexed by its three most intense reflection peaks (at 2θ of 29.96°, 36.34°, and 52.36°, Figures 3a–3d), is the dominant magnetic component in extracts from the four samples with magnetic susceptibility spikes (MSS; Figures 2c and 2j). We define horizons with magnetic susceptibility spikes as "MSS horizons," and other sediments as "host sediments." Chlorite and illite are present as nonmagnetic phases, along with the occasional presence of elemental sulfur in some samples (e.g., sample 38R-2W, 71 cm, Figure 3c). Although the diffraction intensity of the two host sediment samples is generally much weaker, the presence of greigite is still discernible from the three most intense reflection peaks (Figures 3e and 3f). The weak reflection peaks imply that there is a small amount of greigite in the host sediments; this is consistent with their relatively lower magnetic concentration-related magnetic parameters, such as χ and M_s (Figure 2).

Representative SEM images of magnetic mineral extracts are shown in Figure 4. SEM observations indicate that large greigite particles (bright grains, mostly >20 μm; the largest are up to 50–75 μm) are ubiquitous in magnetic extracts from the MSS horizons (Figures 4a, 4c, and 4e–4g). These large greigite particles have a variable (sometimes polyhedral) morphology, probably due to the gentle crushing that was part of the sample preparation procedure. Also, small (cubo-)octahedral greigite particles with variable size (up to ~5 μm) are present (Figures 4b, 4d, and 4h), which resemble the synthetic greigite particles reported by Chang et al. (2007, 2008). In contrast, magnetic extracts from host sediments are dominated by silicates (dark sheets, Figures 4i and 4l), with the presence of only relatively small amounts of fine greigite particles (Figures 4j, 4k, and 4m). Occasionally, hexagonal iron sulfide particles are observed (Figures 4k and 4m), whose morphology is similar to that of monoclinic pyrrhotite (Horng & Roberts, 2006) and smythite (Fe_9S_{11}, Horng et al., 2020). However, it is not sure whether they are pyrrhotite or smythite, because there is no reliable evidence for their presence in XRD results (Figures 3e and 3f).

4.2. SEM/EDS Observations and EPMA Analyses of Thin Sections

SEM observations (Figure 5) and EDS analyses (Table 1) on thin sections reveal that greigite appears to be ubiquitous in all studied sediments, with three typical modes of occurrence. The most impressive mode is as large crystals up to several tens of μm in the MSS horizons (Figures 5a–5d). Most of them have Fe/S atomic ratios close to that of stoichiometric greigite (i.e., ~0.75; Table 1), except for a few spots with Fe/S atomic ratios of ~1 or higher probably due to the low beam voltage (~5 kV) used. The second mode is as laths or small interstitial grains within cleavages of sheet silicate grains (Figures 5e–5h). In some cases, greigite laths are stacked on top of each other, resembling a bunch of bananas (e.g., Figure 5g). The third mode includes aggregates of fine-grained euhedral greigite particles (Figure 5i), which are found occasionally in thin sections. The first two modes are ubiquitous in MSS horizons. In addition, euhedral pyrite grains with Fe/S atomic ratio of ~0.5 (Figure 5j), magnetite grains with varying Ti contents (Figure 5k), and ilmenite (Figure 5l) are occasionally found. EPMA results (Table 1) demonstrate that most of the analyzed grains consist entirely of iron and sulfur, which confirms the dominance of iron sulfides in the studied sediments. Recalculation of the chemical composition on the basis of four sulfur ions reveals that most of the iron sulfide grains are greigite, which is consistent with EDS analyses and XRD diffraction patterns for magnetic mineral extracts (Figure 3). Pyrite (FeS_2) compositions are also identified in some sediments by EPMA (Table 1).

4.3. Rock Magnetism

Anomalously high magnetic susceptibility values (up to ~765×10^{-8} m^3 kg^{-1} on a mass-specific or ~15×10^{-3} SI on a volume-specific basis) are observed in the ~1,103.8–1,108.8 mbsf interval in the Nicobar Fan sequence (Figure 1d and Table 2). This interval contains multiple MSS horizons, which are more evident in the SHMSL magnetic susceptibility measured on archive-half sections (SHMSL κ, Figure 2c). These MSS horizons occur
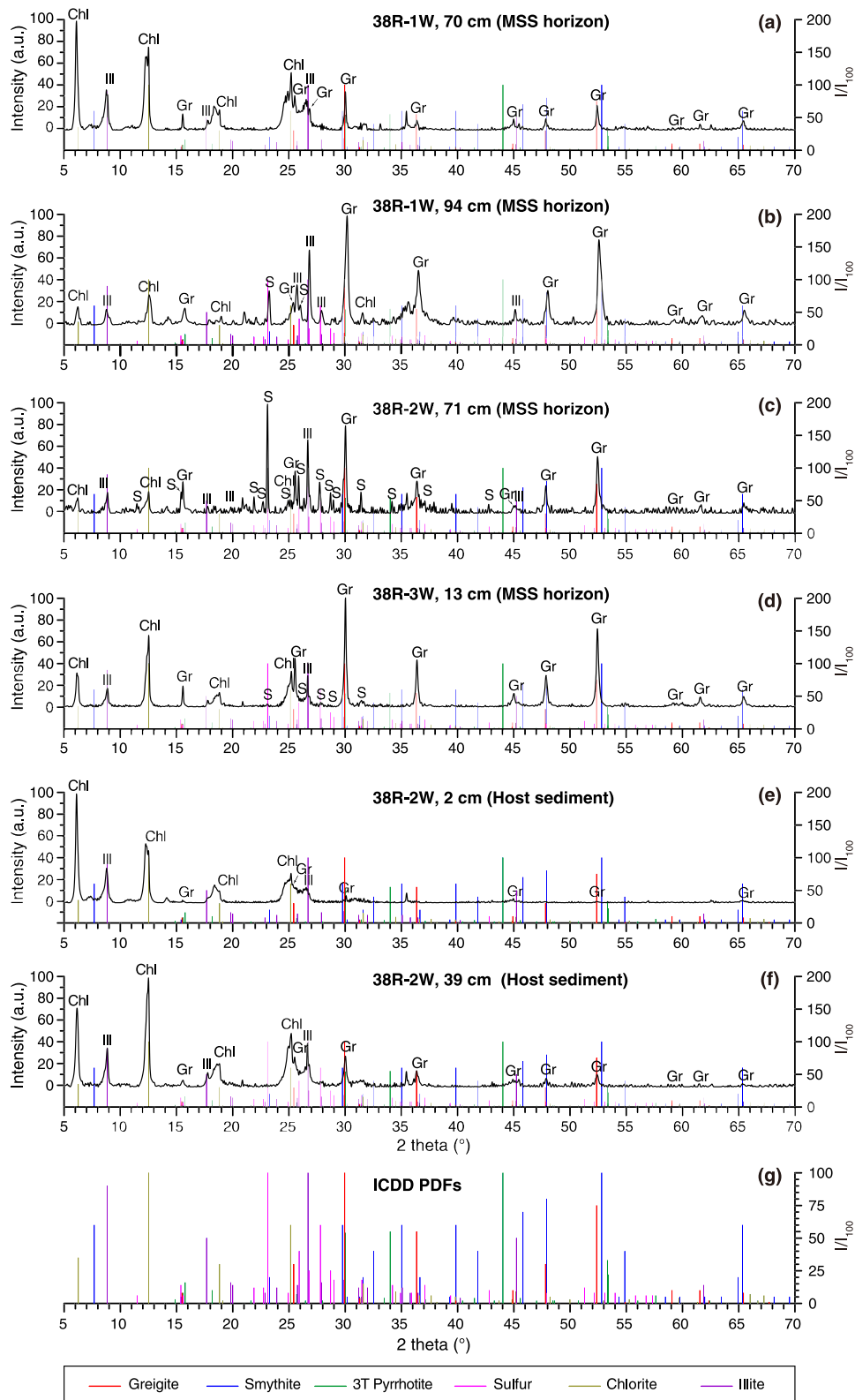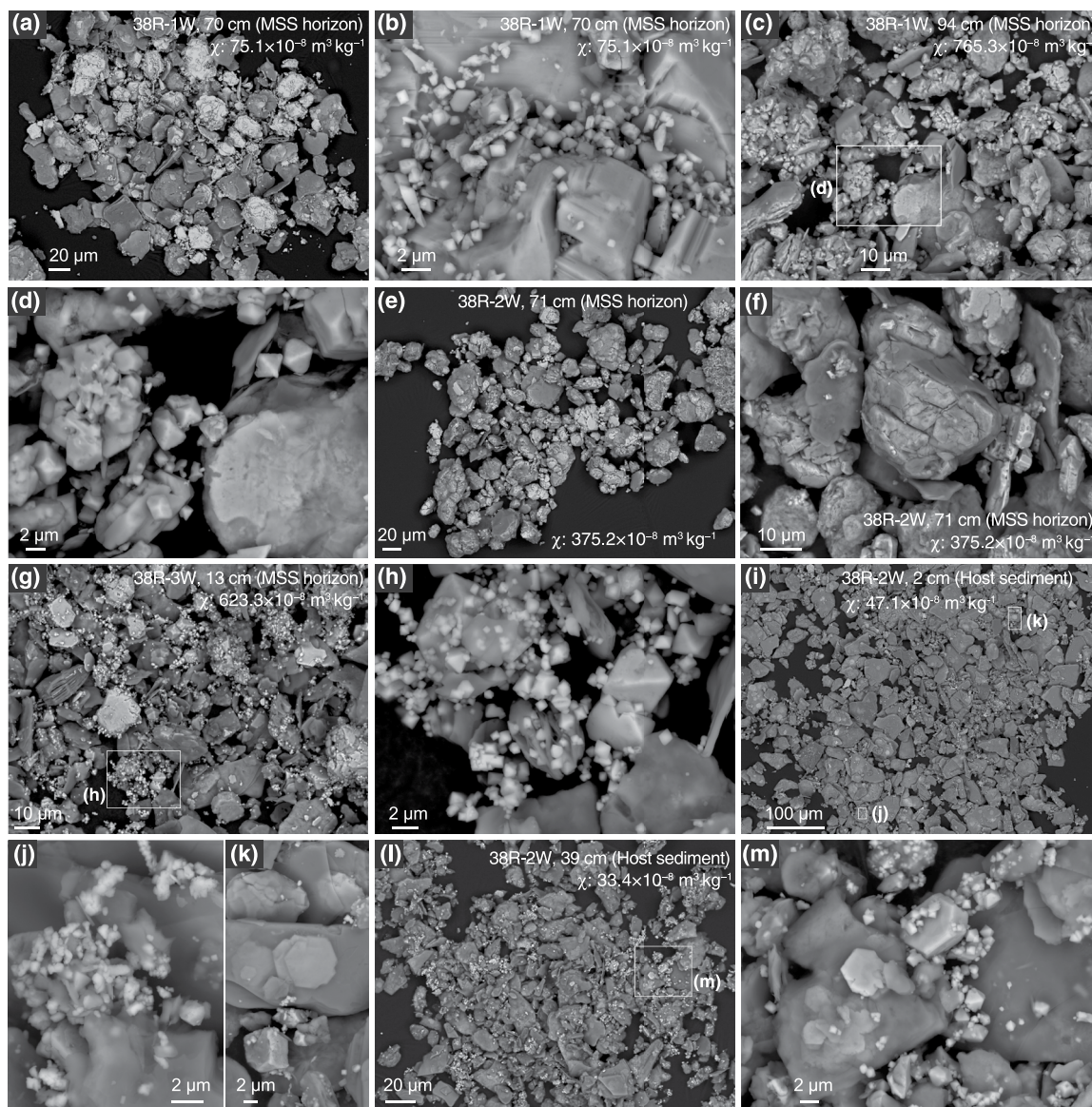
Figure 3.

Figure 4. Backscattered scanning electron microscopy (SEM) images of magnetic mineral extracts from representative sediment samples with different magnetic susceptibilities (χ). As demonstrated by the X-ray diffraction (XRD) spectra (Figure 3), these extracts contain greigite (bright grains) and chlorite/illite (dark sheets). Large greigite particles (mostly >20 μm, with the largest up to 50–75 μm) are ubiquitous in magnetic extracts from the magnetic susceptibility spikes (MSS) sediments (a–h); among them, (cubo-)octahedral greigite particles with variable size (up to ~5 μm) are also present. (i–m) Chlorite/illite sheets dominate extracts from host sediments with lower magnetic susceptibilities, with relatively small amounts of fine greigite particles.

immediately below the most bioturbated horizons (i.e., with BI = 6) located at the top of each turbidite bed (Figures 2a–2c and 2g–2j). The MSS horizons also have high NRM values (Figures 2d and 2k): NRM spikes (>80 × 10⁻³ A/m measured on discrete samples [referred to as NRM-DS] or >40 × 10⁻³ A/m measured on the archive-half sections [referred to as NRM-AHS]) occur, with at least 4 times higher values than typical host sediment NRM (Figures 2d and 2k, and Table 2).

Figure 3. X-ray diffraction patterns of magnetic mineral extracts from representative sediment samples with different magnetic susceptibilities; the extracts contain primarily greigite (Gr), chlorite (Chl), and illite (Ill), along with occasional elemental sulfur (S). Greigite is the dominant magnetic mineral in all magnetic extracts (a–f), as indexed by the first three most intense reflection peaks at 2θ of 29.96°, 36.34°, and 52.36°, respectively. The powder diffraction file (PDF) from the International Centre for Diffraction Data (PDF-4+ 2022) was employed to assist mineral identifications. PDF numbers of minerals are as follows: greigite: PDF 00-016-0713; chlorite: PDF 00-029-0701; illite: PDF 00-026-0911; smythite: PDF 00-010-0437; 3T pyrrhotite: PDF 00-024-0220; and sulfur: PDF 00-008-0247; vertical lines indicate diffraction positions of different minerals and their relative intensities with respect to the largest peak (I/I_{100}) (g).
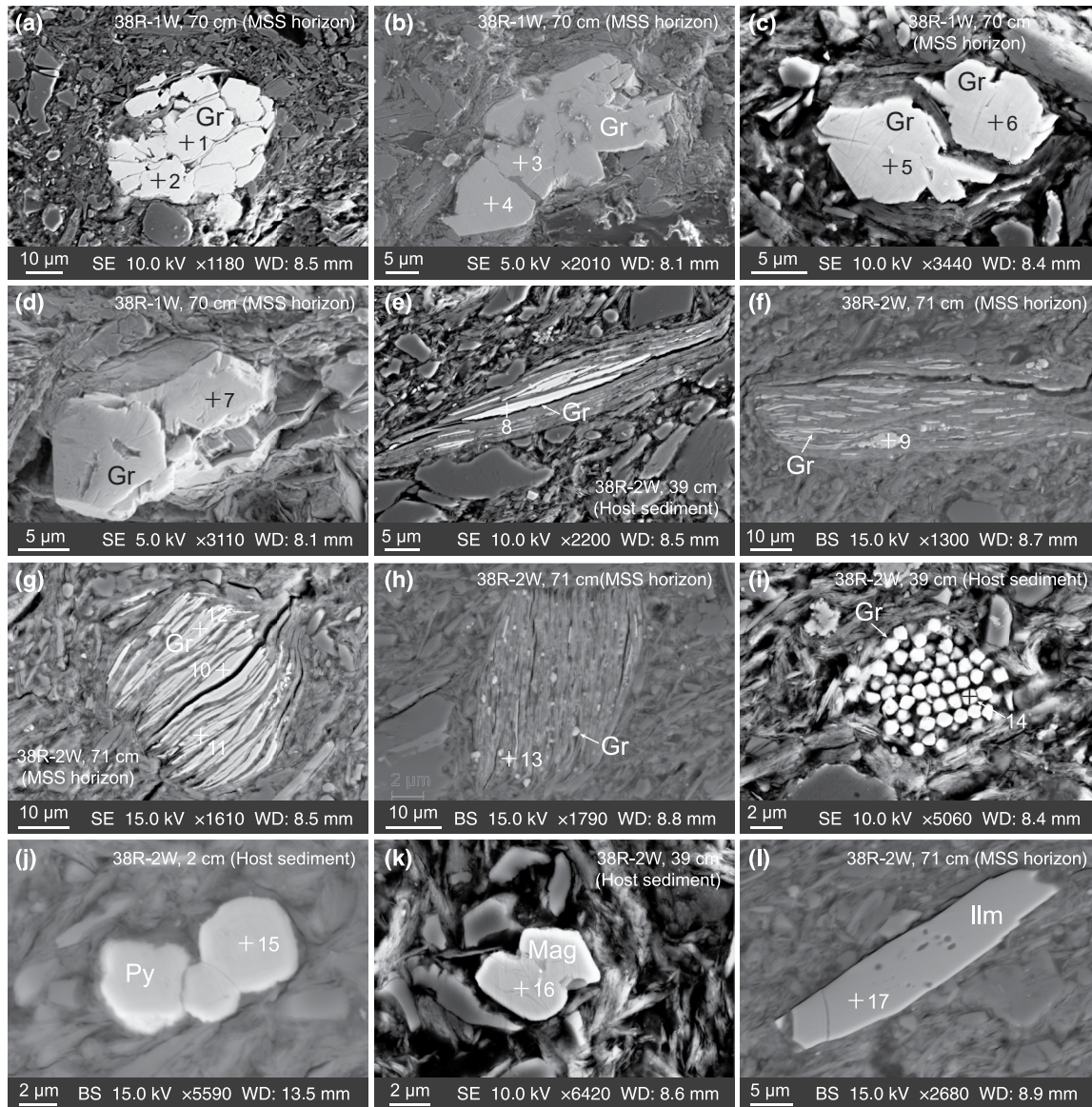
Figure 5. Backscattered (BS) and secondary electron (SE) scanning images of greigite (Gr) microtextures and occurrences in thin sections of selected samples. (a–d) Euhedral greigite particles up to several tens of μm in sediments with magnetic susceptibility spikes (MSS). Greigite (e–g) laths or (h) small interstitial grains within cleavages of detrital sheet silicates; (g) stacked greigite laths, resembling a bunch of bananas; (i) aggregate of fine-grained euhedral greigite crystals; (j) large euhedral pyrite (Py) grains; (k) magnetite (Mag) grains with variable Ti contents; and (l) ilmenite (Ilm). Both the magnetite and ilmenite have rounded edges and are probably of detrital origin. Numbered plus symbols mark the spots of energy dispersive X-ray spectrometry (EDS)/electron probe microanalysis (EPMA) analyses, with detailed results summarized in Table 1.

After high-field slope correction (calculated from magnetizations in fields above 0.7 T), all samples have closed hysteresis loops that approach saturation in a field of ∼300 mT (Figures 6a–6f and Figures S1a–S1c in Supporting Information S1), which indicates that low-coercivity ferrimagnetic minerals are dominant. However, MSS horizons generally have higher M_s and M_{rs}, but lower B_{cr} values compared to host sediments (Figures 2e, 2f and 2l, 2m and Table 2). For example, host sediments have variable M_s (from 4.6 to 47.2×10^{-3} A m^2 kg^{-1}) with an average (±standard deviation) of $22.3 \pm 12.9 \times 10^{-3}$ A m^2 kg^{-1} ($n = 10$). In contrast, M_s of the MSS horizons is much higher, ranging from 37.7 to 873.0×10^{-3} A m^2 kg^{-1} with an average value (±standard deviation) of $337.7 \pm 332.8 \times 10^{-3}$ A m^2 kg^{-1} ($n = 7$; Table 2). MSS horizons have consistently open single-domain (SD)/vortex-state-like hysteresis loops (Figures 6a–6d and Figure S1a in Supporting Information S1); in contrast, the host sediments produce much more potbellied loops (Figures 6e and 6f and Figures S1b and S1c in Supporting Information S1) that are indicative of mixing of stable SD and superparamagnetic (SP) particles (Roberts et al., 2011; Tauxe

Table 1
Chemical Compositions (Unit: wt%) of Typical Magnetic Grains in Thin Sections of Representative Sediment Samples Determined by EDS and EPMA

Spot[a]	EDS											EPMA			
	O	F	Mg	Ti	Al	Si	K	S	Fe	Total	Fe/S[b] (atomic ratio)	Fe	S	Total	Formula[c]
1								42.30	57.70	100	0.78	54.12	42.18	96.30	$Fe_{2.95}S_4$
2								41.87	58.13	100	0.79	53.76	41.54	95.30	$Fe_{2.97}S_4$
3								31.87	68.13	100	1.22	53.39	42.06	95.45	$Fe_{2.91}S_4$
4								38.82	61.18	100	0.90	53.17	41.71	94.88	$Fe_{2.93}S_4$
5								42.61	57.39	100	0.77	52.41	43.06	95.47	$Fe_{2.80}S_4$
6								41.05	58.95	100	0.82	52.71	42.45	95.16	$Fe_{2.85}S_4$
7								33.05	66.95	100	1.16	54.12	42.18	96.30	$Fe_{2.95}S_4$
8								38.44	61.56	100	0.92	50.34	39.04	89.39	$Fe_{2.96}S_4$
9	4.15	2.57				0.44		41.47	51.37	100	0.71				
10	44.77							23.92	31.31	100	0.75	52.91	40.17	93.08	$Fe_{3.02}S_4$
11	3.43	2.81	0.37		0.28	0.64		39.66	52.80	99.99	0.76	49.58	36.75	86.33	$Fe_{3.08}S_4$
12	7.29		0.92		0.65	1.31		37.92	51.90	99.99	0.78				
13	12.16	2.76	0.97		1.23	2.44	0.48	34.34	45.63	100.01	0.76				
14	2.85					0.41		40.26	56.47	99.99	0.80				
15								53.13	46.87	100	0.50	44.15	51.07	95.22	$Fe_{0.99}S_2$
16	31.64			4.22					64.15	100.01	–				
17	35.90			29.62					34.49	100.01	–				

[a]Spot numbers for analyses of each sample are indicated in Figure 5. [b]Chemical compositions for typical magnetic grains revealed by EDS analyses do not coincide precisely with the expected Fe/S atomic ratio of 0.75 for stoichiometric greigite, because the 2 μm electron beam diameter is larger than individual grains under analysis. Analyzed mineral surfaces may also be uneven and the polish quality of resin-impregnated sections can vary. [c]Chemical formulae are calculated based on four sulfur ions for greigite and two sulfur ions for pyrite, respectively, according to the chemical composition determined by EPMA.

et al., 1996). These differences are also highlighted in FORC diagrams (Figures 6g–6l and Figures S1d–S1f in Supporting Information S1). For host sediments, FORC diagrams have closed concentric contours centered on a B_c peak at ~60 mT that are shifted to negative interaction fields (Figures 6k and 6l and Figures S1e and S1f in Supporting Information S1), which indicates strongly interacting stable SD greigite particles (e.g., Roberts et al., 2011), compatible with their hysteresis loops (Figures 6e and 6f and Figures S1b and S1c in Supporting Information S1). However, for FORC diagrams from MSS horizons (Figures 6g–6j and Figure S1d in Supporting Information S1), other than the typical SD peak for greigite in the innermost contour, the inner contours have greater vertical spreading and the outer contours diverge rather than converge at lower coercivities. This suggests the presence of vortex state/multidomain (MD) grains (Lascu et al., 2018; Roberts et al., 2006, 2017, 2018). It is also noteworthy that FORC diagrams for MSS horizons generally have a pronounced "kidney" shape. This points to the cubic anisotropy of greigite as simulated by Valdez-Grijalva et al. (2018). Overall, FORC diagrams for MSS horizons indicate mixed SD and vortex state/MD behavior.

High-temperature thermomagnetic analysis (Figures 6m–6r and Figures S1g–S1i in Supporting Information S1) further reveals the dominant magnetic carrier. Thermal alteration is conspicuous in MSS horizons: a prominent magnetization decay starting at ~250°C and finishing at ~350°C occurs due to thermochemical alteration of greigite to a nonmagnetic phase (Figures 6m–6p and Figure S1g in Supporting Information S1; Chang et al., 2008; Dekkers et al., 2000; Reynolds et al., 1994; Roberts et al., 2011; Torii et al., 1996). This suggests once again that greigite is the predominant magnetic carrier in these samples. In thermomagnetic runs of host sediments (Figures 6q and 6r and Figures S1h and S1i in Supporting Information S1), a similar but relatively weaker change in slope is observed at ~250°C–350°C, and after which a significant fraction of the starting magnetization remains, which indicates the presence of relatively small amounts of greigite. Then, the magnetization decreases further to ~580°C–600°C, which points to the presence of minor magnetite (Dunlop & Özdemir, 1997). The tiny peaks at ~500°C (e.g., Figures 6m–6p and Figure S1g in Supporting Information S1) probably due to the

Table 2
Magnetic Parameters for Discrete Sediment Samples From the Studied Interval (~1,103.80–1,108.80 mbsf) in Hole 1480G, IODP Expedition 362

Sample	Depth (mbsf)	NRM (10^{-3} A/m)	χ (10^{-8} m^3 kg^{-1})	M_s (10^{-3} A m^2 kg^{-1})	M_{rs} (10^{-3} A m^2 kg^{-1})	B_c (mT)	B_{cr} (mT)
MSS horizons ($n = 7$)							
38R-1W, 61 cm	1,104.41	173.9	52.4	48.0	18.1	35.5	53.8
38R-1W, 94 cm	1,104.74	137.5	765.3	369.0	113.3	29.7	49.0
38R-2W, 34 cm	1,105.34	227.1	44.7	37.7	15.2	40.2	58.2
38R-2W, 71 cm	1,105.71	124.4	375.2	873.0	327.1	37.5	54.6
38R-3W, 13 cm	1,106.18	87.3	623.3	701.1	221.8	29.2	47.5
38R-3W, 21 cm	1,106.26	77.1	184.0	248.6	81.1	28.6	46.3
38R-1W, 70 cm	1,104.50	21.6	75.1	86.3	25.2	26.9	47.1
Range		21.6–227.1	44.7–765.3	37.7–873.0	15.2–327.1	26.9–40.2	46.3–58.2
Mean ± Stdev		121.3 ± 67.4	302.8 ± 293.6	337.7 ± 332.8	114.5 ± 119.0	32.5 ± 5.1	50.9 ± 4.6
Host sediments ($n = 11$)							
38R-1W, 18 cm	1,103.98	6.3	24.3	17.3	2.3	13.3	50.7
38R-1W, 88 cm	1,104.68	15.4	33.1	23.3	3.9	18.7	58.5
38R-2W, 2 cm	1,105.02	10.8	47.1	47.2	18.1	36.6	55.4
38R-2W, 39 cm	1,105.39	7.9	33.4	23.5	9.1	40.3	59.2
38R-2W, 76 cm	1,105.76	10.0	35.5	27.9	10.2	37.1	57.6
38R-3W, 6 cm	1,106.11	13.5	41.2	37.0	15.3	40.9	59.4
38R-3W, 46 cm	1,106.51	17.0	27.2	–	–	–	–
38R-4W, 48 cm	1,107.32	26.9	28.8	19.9	7.6	41.6	61.1
38R-4W, 76 cm	1,107.60	1.3	24.5	14.1	3.8	32.8	67.0
38R-5W, 8 cm	1,107.88	2.1	18.4	4.6	0.8	18.4	70.0
38R-5W, 61 cm	1,108.41	3.7	18.2	7.8	2.7	39.8	66.2
Range		1.3–26.9	18.2–47.1	4.6–47.2	0.8–18.1	13.3–41.6	50.7–70.0
Mean ± Stdev		10.4 ± 7.6	30.1 ± 9.0	22.3 ± 12.9	7.4 ± 5.8	31.9 ± 10.8	60.5 ± 5.8

Note. NRM, natural remanent magnetization; χ, mass-specific magnetic susceptibility; M_{rs}, saturation remanence; M_s, saturation magnetization; B_c, coercive force; B_{cr}, remanent coercivity. MSS sediments refer to the sediments with magnetic susceptibility spikes and other sediments to host sediments.

new ferrimagnetic phase (presumably magnetite) produced by Fe-bearing clay minerals or pyrite alteration (Hirt et al., 1993; Just & Kontny, 2012; Passier et al., 2001).

The magnetic mineralogy is further constrained by LT magnetic measurements (Figure 7 and Figures S1j–S1o in Supporting Information S1). For most MSS horizons, no LT phase transition is observed in ZFC/FC (Figures 7b–7d and Figure S1j) and RT-SIRM (Figures 7g–7j and Figure S1m in Supporting Information S1) curves, which concurs with the presence of greigite, although it is not indicative of it (Chang et al., 2009; Roberts et al., 2011). It is noteworthy that the RT-SIRM demagnetizes continuously during cooling to 5 K in the MSS horizons and that irreversible remanence loss (~7%–17%) of the initial SIRM occurs during warming back to room temperature (Figures 7g–7j and Figure S1m in Supporting Information S1), which is a characteristic of vortex state/MD behavior (Chang et al., 2007, 2009). The host sediments and a few MSS horizons (e.g., sample 38R-1W, 70 cm) have a weak Verwey transition (T_v) at ~120 K in ZFC/FC curves (Figures 7a, 7e, and 7f and Figures S1k and S1l in Supporting Information S1) and RT-SIRM curves (Figure 7l and Figures S1n–S1o in Supporting Information S1), which indicates the presence of a small amount of stoichiometric magnetite (Dunlop & Özdemir, 1997). These results corroborate the interpretation of the thermomagnetic behavior. Together, they are consistent with greigite as the dominant magnetic mineral in all of the studied sediments, especially in the MSS horizons, as indicated by the XRD patterns of magnetic mineral extracts (Figure 3). Minor magnetite is also present in the host sediments and occasionally in the MSS horizons. It is also noteworthy that significant remanence "upcurling" is observed below ~20 K in ZFC/FC curves for the host sediments (Figures 7e and 7f and Figures S1k and S1l in Supporting Information S1). This may be indicative of SP grains (Passier &
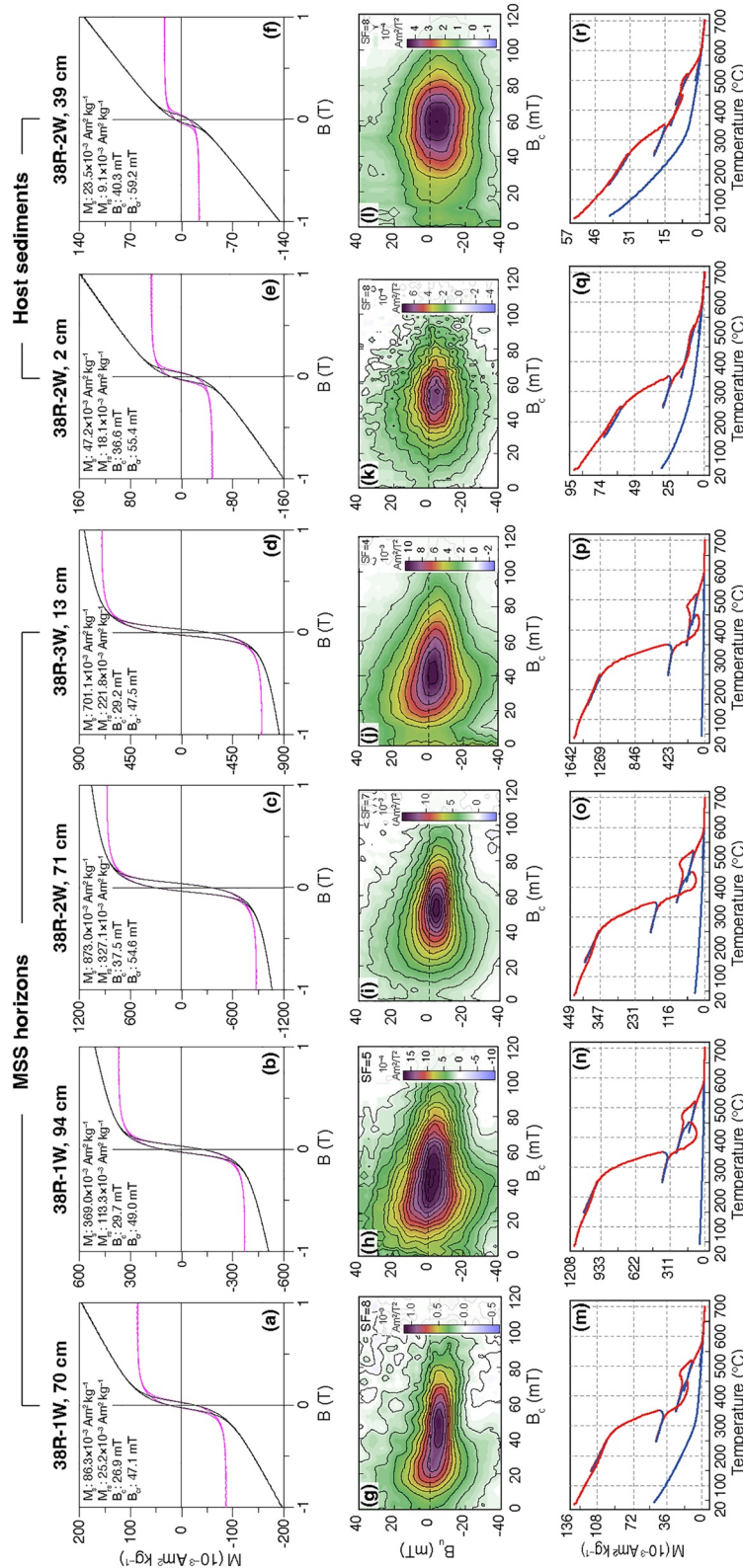
Figure 6. (a–f) Hysteresis loops, (g–l) first-order reversal curve (FORC) diagrams, and (m–r) stepwise thermomagnetic curves for representative samples from the studied interval, Hole U1480G. The hysteresis loops before and after high-field slope correction (using the slope above 0.7 T) are indicated by black and magenta lines, respectively. B, applied field; M, magnetization. FORC diagrams were processed with the FORCinel package (Harrison & Feinberg, 2008) with standard smoothing (Pike et al., 1999). SF, optimal smoothing factor; B_c and B_u are equivalent to a particle coercivity and a local interaction field for single-domain (SD) particles, respectively. Colors in each diagram represent absolute values of the FORC density. Stepwise thermomagnetic analyses in air were performed in a magnetic field that cycled between 100 and 300 mT, with heating/cooling rates of 10°C/min (Mullender et al., 1993). Red (blue) lines indicate heating (cooling) segments. Maximum temperatures of subsequent segments: 150°C, 250°C, 400°C, 520°C, 620°C, and 700°C. Results are for magnetic susceptibility spikes (MSS) horizons; host sediments, other sediments. See Table 2 and Figure 2 for details of sample locations.
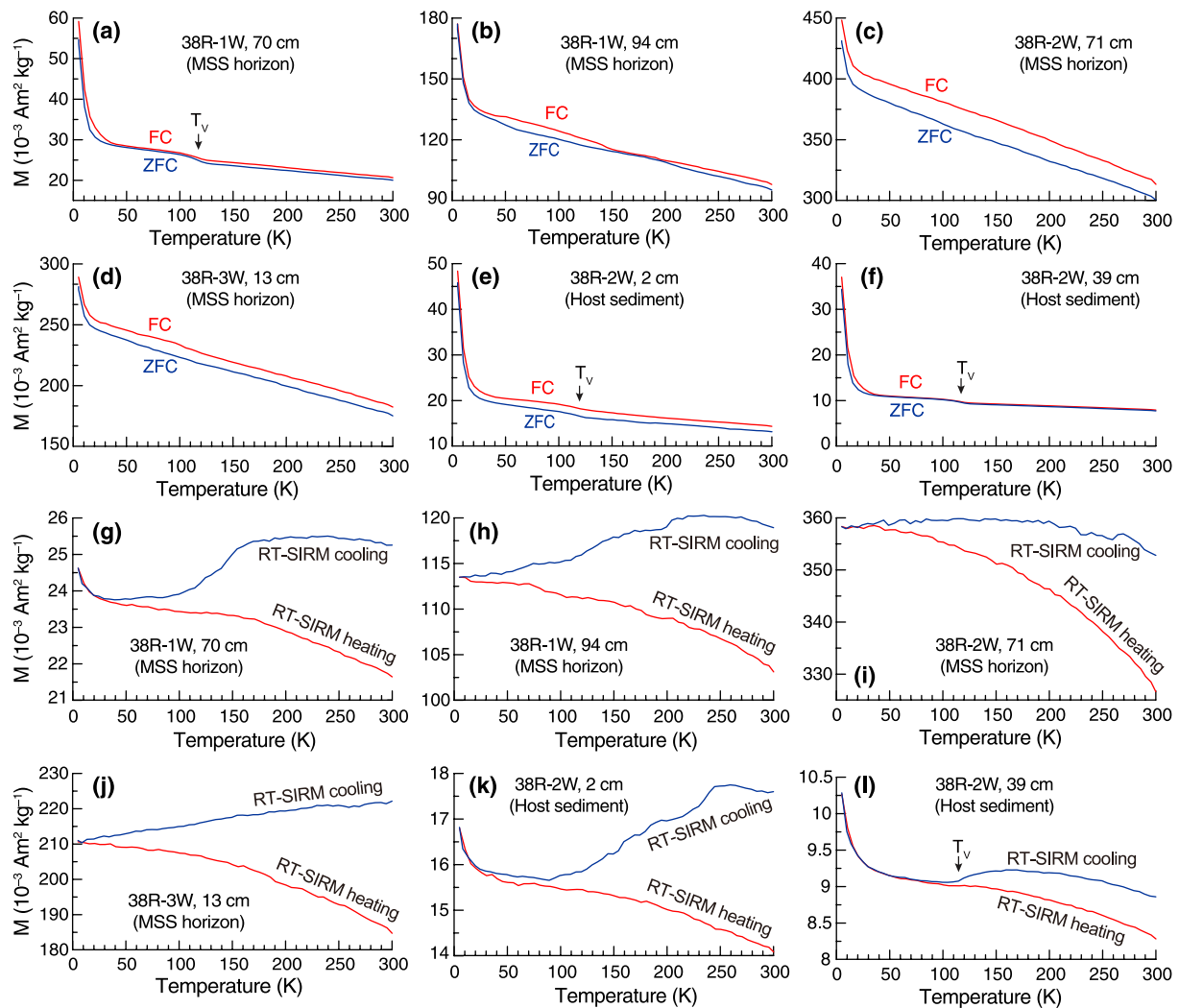
Figure 7. (a–f) Warming curves of a saturation isothermal remanent magnetization (SIRM) imparted to samples in a 2.5 T magnetic field at 5 K. Blue and red curves are ZFC (zero-field-cooled) and FC (field-cooled) runs, respectively. (g–l) Low-temperature cycling curves of a room temperature SIRM (RT-SIRM) imparted to samples in a 2.5 T magnetic field. Blue and red curves are cooling and warming runs, respectively. Arrows with "T_v" indicate the Verwey transition.

Dekkers, 2002; Roberts, 1995), which is compatible with their potbellied hysteresis loops (Figures 6e and 6f and Figures S1b and S1c in Supporting Information S1), although contributions from LT ordering of paramagnetic silicates (clay minerals) in the small residual field of the MPMS cannot be excluded.

4.4. Paleomagnetic Results

For many samples, thermal and AF demagnetization results reveal a low-stability remanence component, which constitutes a small portion of the NRM (Figure 8). Some samples have a (sub)vertical, downward-oriented NRM component, which is easily removed by thermal demagnetization to 100°C–150°C (Figures 8b and 8c) or AF demagnetization to 5–10 mT (Figures 8e–8g and 8i). Such a component is common in drill cores and is considered a drilling-induced overprint (McNeill, Dugan, Petronotis, et al., 2017; Yang et al., 2019). Thermal decay curves of the NRM usually unblock gradually with temperature, and most samples are fully demagnetized at ~350°C (Figures 8a–8d), which further confirms the presence of greigite, as expected from thermomagnetic curves (Figure 6 and Figure S1 in Supporting Information S1). AF demagnetization results have omnipresent "NRM moving-away-from-the-trend-to-the-origin" behavior during AF demagnetization above 50–60 mT (Figures 8e–8i) due to acquisition of gyromagnetic remanent magnetization (GRM; Stephenson, 1980). GRM is also strongly indicative of greigite (e.g., Y. Fu et al., 2008; Roberts et al., 2011; Snowball, 1997). GRM acquisition can be
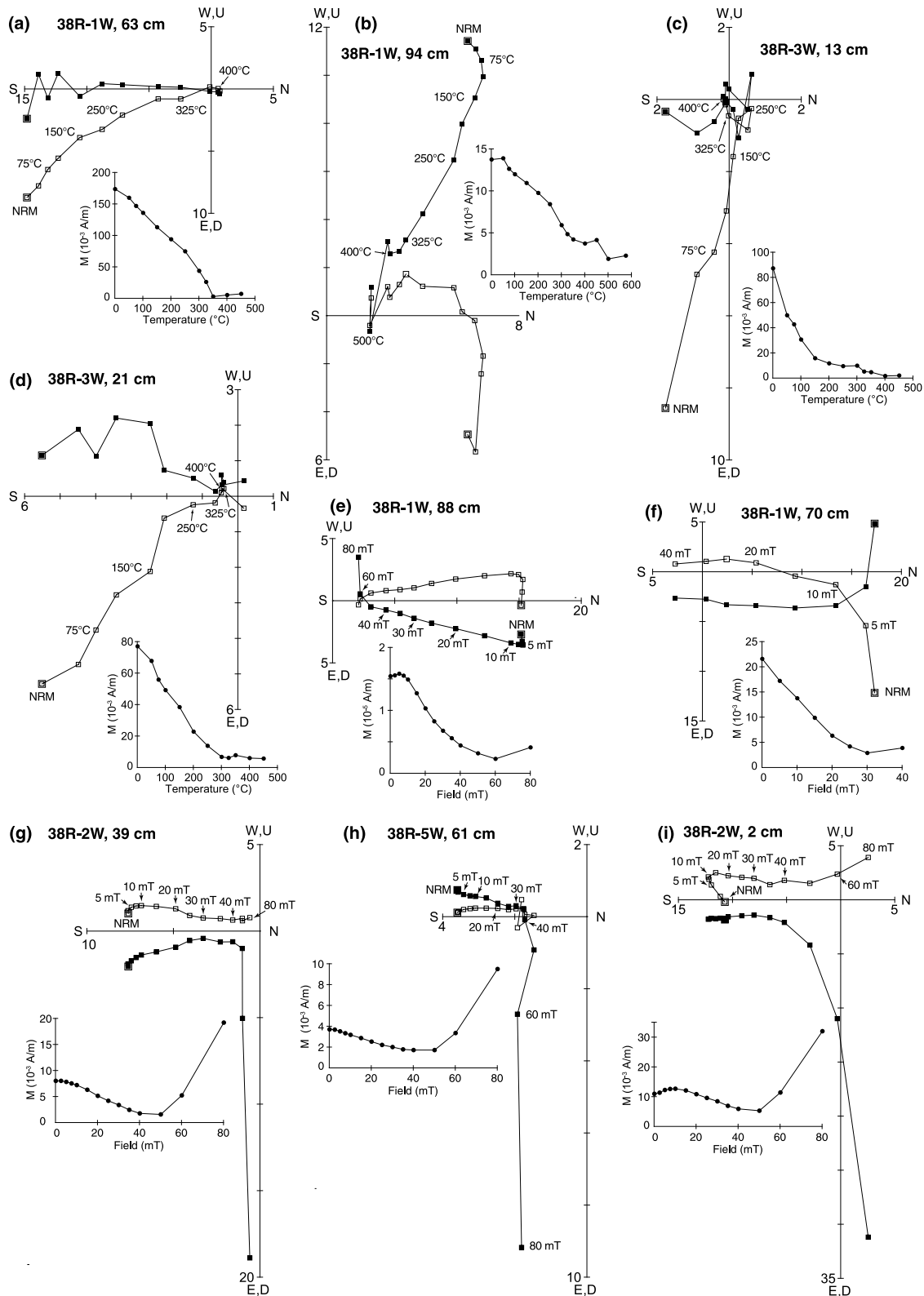
Figure 8. Orthogonal demagnetization diagrams and natural remanent magnetization (NRM) intensity (M) decay curves (insets) for representative samples after stepwise (a–d) thermal demagnetization and (e–i) alternating field demagnetization. Solid and open squares indicate horizontal and vertical plane projections, respectively. Heating steps were 50°C, 75°C, 100°C, 150°C, 200°C, 250°C, 300°C, 325°C, 350°C, 400°C, and 450°C, and peak AF steps were 2.5, 5, 7.5, 10, 15, 20, 25, 30, 35, 40, 50, 60, and 80 mT.

described quantitatively by the ΔGRM/ΔNRM ratio (Y. Fu et al., 2008), where ΔGRM = NRM$_{80mT}$ − NRM$_{min}$ and ΔNRM = NRM$_{0mT}$ − NRM$_{min}$. Our samples have ΔGRM/ΔNRM ratios between 0.14 and 4.82 with an average of 2.34, which suggests a significant GRM contribution due to the presence of large amount of SD greigite in these samples (Y. Fu et al., 2008; Roberts et al., 2011). The greigite particles here are large (mostly >20 μm), especially in MSS horizons (Figures 4 and 5), and far beyond the threshold size for stable SD greigite (i.e., ∼20–200 nm for cubic grains, and ∼20–500 nm for octahedral grains; Roberts et al., 2011). It, therefore, remains unclear whether or to what extent these greigite particles contribute to GRM, or whether the strong GRM is only contributed by SD greigite particles in the studied samples.

Although most samples acquired a GRM at AFs higher than 50 mT, the initial demagnetization steps can still be used to calculate a ChRM. A highly stable magnetization component can be isolated for most of the discrete samples (e.g., Figures 8a, 8b, 8e, and 8g–8i) with PCA (Kirschvink, 1980) for data between 10–15 mT and 40–50 mT or between 150°C and 325°C. Maximum angular deviation values are mostly <10°, and often <5° (see Table S1 for details). Only a few samples, especially those subjected to thermal demagnetization, have incoherent demagnetization behavior and random remanence directions (e.g., Figure 8c). These high-coercivity components all have reversed polarity and their inclinations are mostly concentrated at −9° ± 7°.

4.5. TOC and TN Contents

The typical TOC background value is <0.6 wt% with an average of 0.37 ± 0.18 wt% (n = 334; Figure 9a), while TN is typically <0.1 wt% with an average of 0.06 ± 0.02 wt% (n = 334; Figure 9b) throughout Site U1480 (House, 2019). TOC in the studied interval ranges from 0.44 to 0.84 wt% with an average of 0.60 ± 0.13 wt% (n = 14; Figure 9d), while TN ranges from 0.08 to 0.14 wt% with an average of 0.11 ± 0.02 wt% (n = 14; Figure 9e), which is much higher than typical background values. It is also noteworthy that the MSS horizons generally have relatively low TOC but are enriched in TN (Figures 9c–9e).

5. Discussion

5.1. Occurrence of Large Greigite Particles in Bioturbated Turbidites

The above-mentioned rock magnetic and paleomagnetic results reveal distinct magnetic behavior in the studied sediments, including the negative slope of FORC distributions, thermal alteration above ∼250°C during heating, lack of a LT magnetic transition, and GRM acquisition during AF demagnetization (Figures 6–8 and Figure S1 in Supporting Information S1). All of these observations together point to the presence of greigite as the most likely dominant magnetic mineral. However, the authigenic 3T pyrrhotite (Fe$_7$S$_8$) polytype (Horng, 2018; Horng & Roberts, 2018) and smythite (Fe$_9$S$_{11}$; Horng et al., 2020) also have similar magnetic behavior. The overlap of magnetic properties of iron sulfides (i.e., greigite, smythite, and 3T pyrrhotite) makes their identification challenging through mineral magnetic means.

Nevertheless, 3T pyrrhotite is reported to have a higher B_c (>100 mT at room temperature; Horng, 2018; Horng & Roberts, 2018) compared to natural greigite with typical B_c values of 40–60 mT (Roberts, 1995; Roberts et al., 2011). Here, the studied sediment samples have average B_c values between 13 and 42 mT with an average of ∼32 mT (Table 2), which is much lower than that of 3T pyrrhotite. On the other hand, among these three magnetic iron sulfide minerals, 3T pyrrhotite has the weakest magnetization, followed by smythite, while greigite has the strongest magnetization (Horng, 2018; Horng & Roberts, 2018). M_s for sediments from the MSS horizons ranges from 37.7 to 873.0 × 10^{-3} A m^2 kg^{-1} with an average of 337.7 ± 332.8 × 10^{-3} A m^2 kg^{-1} (Table 2). Taking 10.3 and 3 A m^2 kg^{-1} as M_s estimates for smythite (Hoffmann et al., 1993; Horng et al., 2020) and 3T pyrrhotite (Horng & Roberts, 2018), respectively, these sediments would contain 0.37–8.5 wt% (with a mean of 3.28 ± 3.23 wt%) smythite or 1.26–29.1 wt% (with a mean of 11.3 ± 11.1 wt%) 3T pyrrhotite to produce the observed high M_s values in the MSS horizons (Figure 2 and Table 2). Such high concentrations of smythite or 3T pyrrhotite seem unlikely in marine sediments and would have been detected by XRD analysis. This suggests that neither smythite nor 3T pyrrhotite would be the main magnetic carrier in the studied sediments. Importantly, our nonmagnetic analyses, including XRD analysis and SEM/EDS observations of magnetic extracts, and SEM/EDS observations and EMPA analyses of thin sections provide strong evidence for greigite rather than smythite or 3T pyrrhotite in the studied sediments (Figures 3–5 and Table 1). The possibility that 3T pyrrhotite and/or smythite occur between chlorite sheets cannot be fully precluded. However, if present they apparently occur
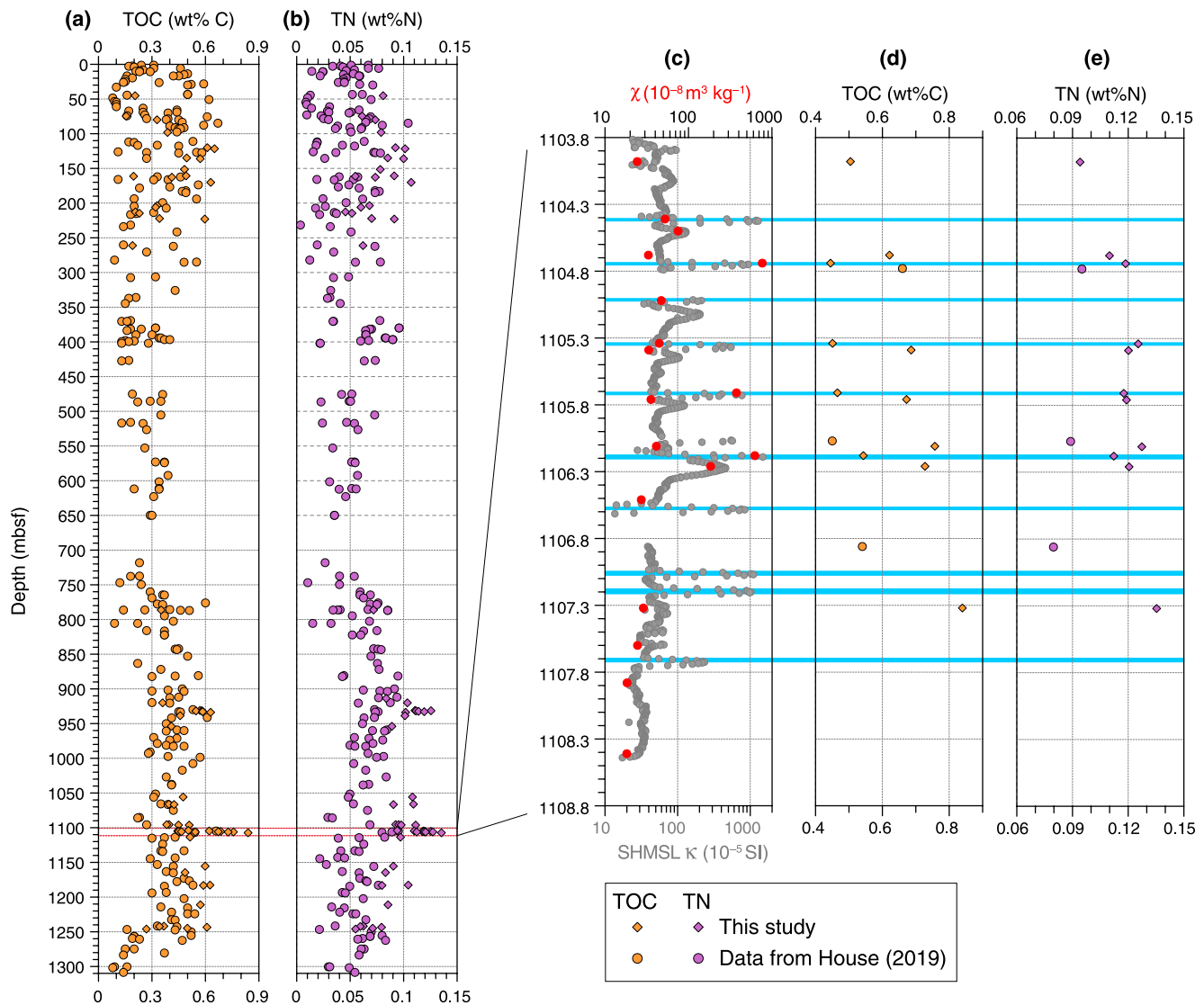
Figure 9. Downhole (a) total organic carbon (TOC) and (b) total nitrogen (TN) of sediments from Site U1480. Close-up views of the ~1,103.8–1,108.8 mbsf interval are shown in (d) and (e), with (c) comparison to magnetic susceptibility (χ). Blue bars mark MSS horizons. Diamonds: data collected in this study; dots: data from House (2019).

only in trace amounts. Therefore, the combination of above-mentioned mineral magnetic properties, paleomagnetic demagnetization behavior, microscopic observations, and chemical composition data provides compelling evidence that all of the studied sediments are dominated magnetically by greigite with variable size and distinct morphology, with minor magnetite in the host sediments. It is also worth mentioning that lath-shaped magnetic iron sulfide particles (Figures 5e and 5g) are identified here for the first time as greigite; such morphologies have previously been misinterpreted as monoclinic pyrrhotite and are likely to be a different authigenic phase (e.g., Roberts, 2015; Roberts et al., 2010, 2011; Weaver et al., 2002). Lath-shaped 3T pyrrhotite polytype has also been reported (Horng, 2018; Horng & Roberts, 2018). Each of these minerals likely requires specific formation conditions. Future work is needed to understand the sedimentary conditions in which lath-shaped greigite and other iron sulfides form.

The remanent coercive force B_{cr} could be a first-order grain-size indicator for natural greigite in sedimentary settings, with the general "ferrimagnetic" rule from SD upward in size: the coarser the grain size, the lower the B_{cr} (Dunlop & Özdemir, 1997). B_{cr} values in the MSS horizons are between 46 and 58 mT with an average of 50.9 mT ($n = 7$; Table 2; Figure 10a), which is at the low end of the range reported for natural greigite (i.e.,
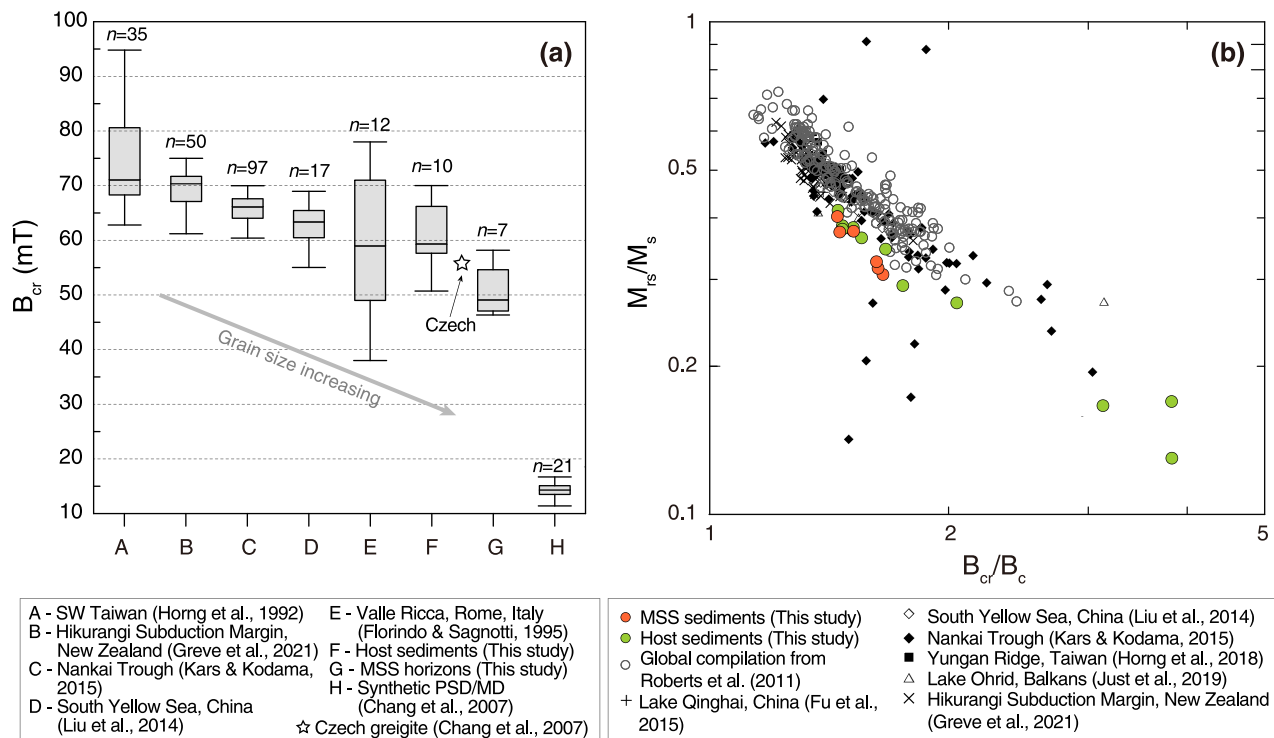
Figure 10. (a) Comparison of B_{cr} values from this study with those reported for natural sedimentary greigite from SW Taiwan (Horng et al., 1992), Hikurangi Subduction Margin, New Zealand (Greve et al., 2021), Nankai Trough (Kars & Kodama, 2015), South Yellow Sea, China (J.-X. Liu et al., 2014), Valle Ricca, Rome, Italy (Florindo & Sagnotti, 1995), Czech Republic (Chang et al., 2007), and synthetic greigite (Chang et al., 2007). (b) Bilogarithmic plot of the hysteresis ratios M_{rs}/M_s and B_{cr}/B_c of sediments from this study, compared to published hysteresis data for greigite from a global compilation by Roberts et al. (2011), South Yellow Sea, China (J.-X. Liu et al., 2014), Lake Qinghai, China (C.-F. Fu et al., 2015), Yungan Ridge, Taiwan (Horng, 2018), Lake Ohrid, Balkans (Just et al., 2019), and Hikurangi Subduction Margin, New Zealand (Greve et al., 2021).

45–95 mT) and demonstrated by SD greigite (Roberts, 1995; Roberts et al., 2011). Values are notably higher than those reported for synthetic vortex state/MD greigite (i.e., 11–19 mT) with mean grain sizes from <4 to 13 μm (Chang et al., 2007). However, our B_{cr} values are much lower than B_{cr} values for SD greigite-bearing sediments from other regions worldwide, such as southwestern Taiwan (Horng et al., 1992), Hikurangi Subduction Margin, New Zealand (Greve et al., 2021), Nankai Trough (Kars & Kodama, 2015), South Yellow Sea, China (J.-X. Liu et al., 2014), and Valle Ricca, Rome, Italy (Florindo & Sagnotti, 1995), which range between 60 and 86 mT (Figure 10a). It is also lower than that of Czech greigite from Miocene coal-bearing lacustrine sediments (~56.3 mT; Chang et al., 2007), which is 4–8 μm in size and has MD-like magnetic properties (Hoffmann, 1992). This suggests that greigite in the MSS horizons is much coarser than widely reported natural greigite. This is further illustrated with a bilogarithmic plot of M_{rs}/M_s versus B_{cr}/B_c (Figure 10b), in which MSS horizons and host sediments have different distributions: most of the host sediments lie along the widely reported natural greigite data "cloud," whereas data for some of the MSS samples plot far below it. This is indicative of different magnetic domain states for them. Natural greigite particles are often less than a few hundred nanometers in size (e.g., Lesniak et al., 2021 and references therein). Thus, in most sediments, greigite is in the SP or SD state; MD behavior has only been reported rarely for natural greigite (Pósfai et al., 2001; Roberts et al., 2011). Until now, the coarsest natural greigite reported seems to be the above-mentioned greigite from the Czech Republic (Krs et al., 1990). In contrast, here the MSS horizons contain abundant coarse-grained greigite particles with sizes up to ~50–75 μm (Figures 4 and 5).

5.2. A New Greigite Formation Pathway

The most important determinants for greigite formation and preservation in reducing sedimentary environments are the amount of biologically degradable organic matter and reactive iron, as well as the availability of dissolved sulfate that is biologically reduced to sulfide by sulfate-reducing microorganisms (Berner, 1984; Blanchet
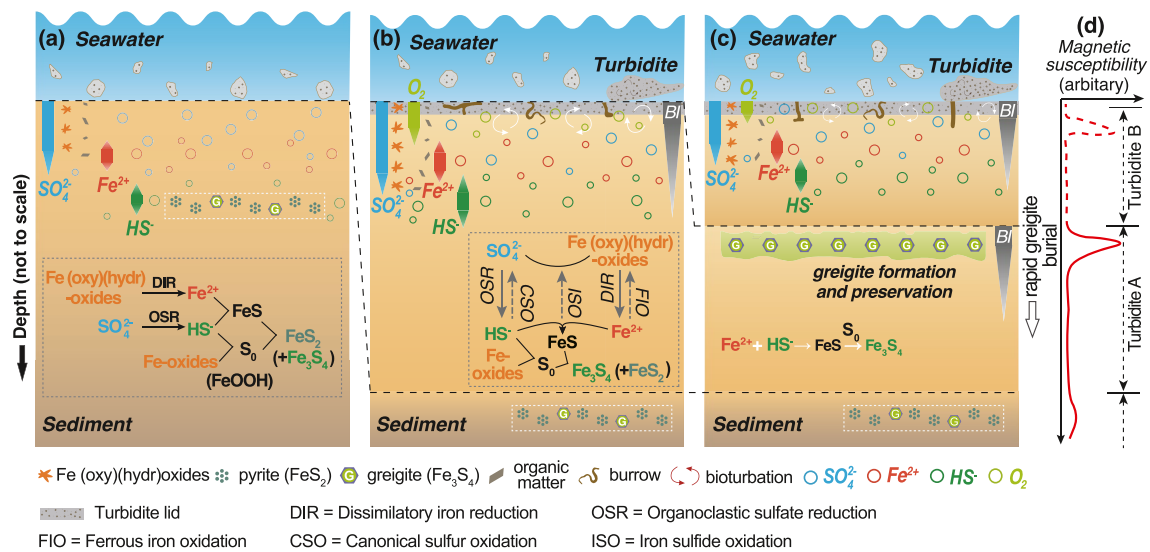
Figure 11. Conceptual model for the greigite-rich layers formation and preservation modulated by turbidites and bioturbation. (a) Under steady state conditions in anoxic sediment, reductive dissolution of detrital iron (oxy)(hydr)oxide minerals releases dissolved Fe^{2+} into pore waters, where it reacts readily with upward diffusing hydrogen sulfide (HS^-) produced by organoclastic sulfate (SO_4^{2-}) reduction (OSR). This leads to iron monosulfide (FeS) precipitation, which subsequently reacts with sulfur (S_0) produced by direct reactions of iron oxides with HS^- to yield pyrite (FeS_2) with intermediate greigite (Fe_3S_4). Transformation of ferrimagnetic/ antiferromagnetic iron (oxy)(hydr)oxides into paramagnetic pyrite results in a magnetic susceptibility decrease. (b) Deposition of organic-rich turbidites disrupts steady state conditions. Intensive bioturbation causes downward transport of previously buried organic matter, iron (oxy)(hydr)oxides, and SO_4^{2-}. Upward diffusion of HS^- and Fe^{2+} in pore waters also occurs. Once in contact with O_2 at/near the sediment–water interface, they are (partially) reoxidized with formation of additional iron (oxy) (hydr)oxides and SO_4^{2-}, respectively. These lead to enrichment of organic matter and iron (oxy)(hydr)oxides, Fe^{2+}, and HS^- and/or SO_4^{2-} at the top of the turbidite bed. (c) The ensuing mud-rich turbidite pulse quickly buried the previous turbidite bed and creates closed system conditions. Rapid pore water SO_4^{2-} consumption via microbially mediated OSR leads to pore water SO_4^{2-} depletion and production of dissolved HS^-. Due to the relatively abundant reactants, plentiful Fe^{2+} and HS^- can be supplied to favor iron monosulfide (FeS) formation. Once supply of Fe^{2+} exceeds HS^-, the pyritization process is arrested and intermediate greigite is preserved. With successive turbidite pulses, multiple greigite-rich layers form in intensely bioturbated horizons at the tops of turbidite beds, resulting in multiple sedimentary magnetic susceptibility spikes (d). See main text for details. Cartoons partially refer to Lin et al. (2021).

et al., 2009; Chang et al., 2014; Kao et al., 2004; Roberts, 2015). In marine sedimentary sequences, sulfate is omnipresent and pyrite (FeS_2) is typically the end-product of sulfate reduction during diagenesis. Steady state diagenetic conditions are often interrupted by, for example, temporally variable organic matter input and sedimentation rate changes (Roberts, 2015). This may lead to arrest of the pyritization process, favoring the greigite formation and preservation. Other than greigite magnetosomes produced by magnetotactic bacteria (e.g., Kopp & Kirschvink, 2008) and biologically induced extracellular greigite as a by-product of sulfate-reducing bacteria (e.g., Watson et al., 2000), several pathways for authigenic greigite formation have been documented (e.g., Roberts, 2015). They include neoformation of greigite on surfaces of early pyrite, authigenic clays (smectite, illite), siderite, and gypsum, or within cleavages of detrital sheet silicate grains (Florindo et al., 2007; Jiang et al., 2001; Roberts & Weaver, 2005). In the cored sequence, abundant coarse-grained greigite is confined to multiple horizons of structureless mudstone immediately below the most bioturbated intervals at top of the muddy TOC-rich turbidite beds (Figures 3–5 and 9). Reported sedimentary greigite formation pathways do not cover this mode of occurrence, which suggests the need to further explore greigite formation pathways that would lead to the large crystal sizes as in the present study.

Based on the mineral magnetic signatures recorded in the studied bioturbated turbidites, a conceptual model is proposed to illustrate the modulation of turbidites and bioturbation on greigite formation and preservation (Figure 11). Since ~9.2 Ma, rapid exhumation in the broad Himalayan syntaxial region led to increased erosion of the Greater Himalaya (McNeill, Dugan, Backman, et al., 2017; Pickering et al., 2020). Thus, a large terrigenous sediment load was delivered to the Nicobar Fan by rivers, primarily the Brahmaputra River (W.-H. Chen et al., 2020). The Nicobar Fan sediments studied here have relatively high TOC contents (Figure 9d), implying that turbidite deposition introduced an external organic matter input. This would disrupt steady state conditions, under which pyrite is the foremost product of sulfidic diagenesis with the occasional presence of fine-grained greigite (Figure 11a). Benthic fauna bioturbate and rework sediments, thereby facilitating sediment–pore–water interactions. Intensive bioturbation would cause downward transportation of reactive compounds like previously buried

organic matter, iron (oxy)(hydr)oxides, and sulfate through biological mixing (Figure 11b; e.g., Aller, 1994; Canfield & Farquhar, 2009; van de Velde & Meysman, 2016). Intensive bioturbation also promotes upward movement of sulfides from the underlying sediments, and upward diffusion of Fe^{2+} in pore waters. Free Fe^{2+} and sulfides could then be (partially) reoxidized with formation of additional iron (oxy)(hydr)oxides and sulfate, respectively, when they come into contact with O_2 at the top of the turbidite bed and/or are recycled repeatedly near the sediment–water interface (Figure 11b; Anderson & Raiswell, 2004; Y. Wang et al., 2019; Wijsman et al., 2001). Fecal pellets and carcasses of these benthic bioturbating fauna would represent a further organic matter input to the sediments. All of these induce enrichment of organic matter, iron (oxy)(hydr)oxides, Fe^{2+}, and sulfides and/or sulfate in intensively bioturbated horizons at the top of turbidite beds.

The ensuing muddy-rich turbidite pulse rapidly buried the previous turbidite bed, which would cut off the downward oxygen flux and lead to a closed diagenetic system (Figure 11c). This "coffin-lid" effect facilitates rapid buildup of reducing conditions within sediments immediately below a turbidite (Anschutz et al., 2002; Deflandre et al., 2002; de Lange, 1986, 1998; McKay & Pedersen, 2014; Raiswell et al., 2008; Robinson, 2001; Robinson & Sahota, 2000; Schimmelmann, 2011; Thomson et al., 1993, 1998; Volvoikar et al., 2020). Other similar quasi-instantaneous depositional events, such as floods (e.g., Tesi et al., 2012; Y. Wang et al., 2019), can also cause punctuated redox changes. The sediments of interest here are enriched in organic matter and iron (oxy)(hydr)oxides, Fe^{2+}, and sulfides and/or sulfate as discussed above. In such closed system conditions, rapid porewater SO_4^{2-} consumption via OSR (Berelson et al., 2019; Burdige, 2006; Claypool, 2004; X. Liu et al., 2019; Shaw & Meyers, 1996; Thomson et al., 1993, 1998; Volvoikar et al., 2020) leads to pore water SO_4^{2-} depletion and production of dissolved HS^- (e.g., Canfield, 2001). Due to the relatively high stock of reactants, abundant Fe^{2+} and HS^- can be supplied and favor iron monosulfide formation (Figure 11c). Once the Fe (oxy)(hydr)oxide reduction outpaces sulfide production from microbial sulfate reduction (when porewater sulfate is consumed completely) and supply via diffusion, a surplus of Fe^{2+} over HS^- is created. This will arrest the ongoing pyritization process, and greigite will be preserved as an intermediate (Kao et al., 2004). This is also supported by the (almost complete) lack of pyrite in the MSS horizons, which indicates that pyrite growth was effectively stopped by the burial conditions combined with the high sedimentation rate (∼220 m/m.y.; e.g., van Baak et al., 2016). It may be that the prolonged small degree of supersaturation of Fe^{2+} and HS^- in such a quasi-closed system favors the growth of greigite crystals to larger particles, because the free energy for crystal growth is typically lower than that for crystal nucleation (i.e., forming new "seed" crystals). For pyrite, the degree of supersaturation in solution is the primary factor controlling its morphology (e.g., Murowchick & Barnes, 1987; Q. Wang & Morse, 1996). However, no data on crystal growth versus supersaturation exist yet for greigite, which precludes specific statements. This warrants further geochemical work. Accumulation of large amounts of coarse-grained greigite significantly elevates the magnetic susceptibility (Figure 11d). Similar diagenetic magnetic enhancement has been reported for organic-rich sapropels from the eastern Mediterranean Sea (Larrasoaña et al., 2003; Roberts et al., 1999) and Baltic Sea (Reinholdsson et al., 2013).

It is noteworthy that lower TOC values in the studied intervals generally coincide with MSS (Figures 9c and 9d). This may imply that a large amount of organic carbon was consumed during the sulfate reduction process to supply hydrogen sulfide for intermediate iron monosulfide formation. This (anti)correlation further highlights the control of the amount of organic matter on greigite production and preservation (e.g., Kao et al., 2004; J. Liu et al., 2005; J.-X. Liu et al., 2018). The presence of greigite in the upper portion of each turbidite bed, therefore, is attributed to insufficient sulfate supply resulting from enhanced organic matter and Fe (oxy)(hydr)oxide input by successive turbidite pulses, which were significantly reworked by intensive bioturbation. Nitrate (NO_3^-) can oxidize FeS back to ferric iron and induce incomplete iron monosulfide oxidation to form greigite (Y. Fu et al., 2008; Schippers & Jørgensen, 2002). Therefore, here the anomalously high TN content (Figure 9e) may also have contributed to greigite formation to some extent.

5.3. Implications for Paleomagnetic Studies and Fe–S–C Cycling

The most important impact of authigenic greigite on sedimentary magnetizations is the partial or even complete overprinting of the primary (paleo)magnetic signal due to partial or complete detrital iron oxides dissolution. Greigite formation, thus, leaves a secondary paleomagnetic signal in host sediments. Only when greigite formation can be shown to be early diagenetic, that is, quasi-primary, can paleomagnetic records involving greigite be considered trustworthy (Roberts et al., 2011), especially for classic paleomagnetic and magnetostratigraphic

studies. The suitability of greigite-bearing strata for high-resolution geomagnetic field studies, like paleosecular variation studies, remains questionable. The timing of greigite formation, which varies greatly with the availability of dissolved sulfide and iron, is the key issue for assessing the fidelity of the paleomagnetic record carried by greigite (Roberts & Weaver, 2005).

As shown in demagnetization diagrams of representative samples (Figure 8), a stable ChRM can be isolated for most of the studied sediments (Table S1), and all have reversed polarity with inclinations mostly concentrated at $-6.7°$ with $\alpha_{95} = 5.5°$. This suggests that the samples maintained an inclination close to the expected geocentric axial dipole field inclination ($-5.2°$) for the drill site latitude at ~8.6 Ma in the Late Miocene (approximately $\sim2.6°$N, following the Indian Plate motion model of Acton [1999]). Magnetite, which has reductive dissolution half-lives that range from 72 days (Poulton et al., 2004) to 105 years (Canfield et al., 1992) depending on reaction conditions, is not detected in the MSS horizons. This implies rapid magnetite dissolution to release Fe^{2+}. Release of Fe^{2+} sorbed onto silicate layers is expected to be a more important Fe^{2+} source from a mass balance viewpoint than the few per mil of magnetite. The dissolved Fe^{2+} reacts with dissolved sulfide to form iron sulfides during early diagenesis as discussed above (Figure 11; e.g., Berner, 1984; Hüsing et al., 2009). Also, greigite occurs here dominantly as large particles, laths, and only occasionally as fine-grained euhedral greigite crystal aggregates (Figures 4 and 5). In contrast, greigite produced by slow late diagenetic reactions, such as between the cleavages of detrital sheet silicates (e.g., Figure 5h; Canfield et al., 1992; Jiang et al., 2001; Passier & de Lange, 1998; Raiswell & Canfield, 1996; Roberts & Weaver, 2005; Roberts, 2015), is not so common in the studied sediments (Figure 5). Overall, these observations suggest that the coarse-grained greigite formed in an early stage after deposition. Vortex state greigite grains (≥70 nm) can be expected to carry a stable magnetization over billion-year timescales (Valdez-Grijalva et al., 2018). Here, the turbidite and bioturbation-modulated greigite particles have crystal sizes up to ~10–20 μm (Figures 4 and 5), with dominantly SD/vortex state behavior (Figure 6). It is, thus, conceivable that the newly formed greigite recorded a (quasi-)primary near-syn-sedimentary paleomagnetic signal. Similar cases have been reported in Dallas, TX (USA; Reynolds et al., 1999), Black Sea (Chang et al., 2014; Cutter & Kluckhohn, 1999; J.-B. Liu et al., 2018), eastern New Zealand (Rowan & Roberts, 2006), northern Italy (Hüsing et al., 2009), Santa Barbara basin (Blanchet et al., 2009; Y. Wang et al., 2019), and southeastern Romania (S.-Z. Liu et al., 2017; Palcu et al., 2015; Vasiliev et al., 2007).

From another perspective, our observations highlight the role of enhanced sulfur burial through the pathway of greigite formation and preservation in bioturbated turbidite fan sediments (Otero et al., 2003; Riedinger & Brunner, 2014; Shaw & Meyers, 1996; Taillefert et al., 2017; Yucel, Konovalov, et al., 2010; Yucel, Luther, et al., 2010). This may have important implications for the global Fe–C–S cycle. In the MSS horizons, the greigite content is estimated to range between 0.06 and 1.30 wt% with a mean of 0.50 ± 0.50 wt%, by comparing measured M_s values (Table 2) to that of pure greigite (67.17 A m^2 kg^{-1}; Li et al., 2014). This implies that the samples contain at least ~0.04–0.94 wt% Fe and ~0.02–0.36 wt% S, respectively, with Fe and S in pyrite and Fe in other minerals not included. At the deformation front offshore of North Sumatra, the Nicobar Fan sediments are as thick as 4–5 km (McNeill, Dugan, Backman, et al., 2017; McNeill, Dugan, Petronotis, et al., 2017; Pickering et al., 2020). Bioturbated turbidites are common facies in the Nicobar Fan (Pickering et al., 2020), thus, greigite appears to be an important Fe and S sink.

Similar fan sediments (e.g., Congo, Bengal, and Indus Fans) should be considered globally significant iron–sulfur sinks which are coupled with high loadings of organic carbon. Submarine fans generally have enormous areas, with appreciable thicknesses. Bioturbation has been documented widely in turbidites from the late Cambrian to early Ordovician times (e.g., Crimes & Fedonkin, 1994). The global volume of bioturbated sediment is estimated to be up to 20,700 km^3 per year (Teal et al., 2008), which implies that bioturbation is the norm in many deep-sea floor areas (including these deep-sea fans). It also is a foremost important factor controlling the biogeochemical cycling of iron and sulfur (e.g., van de Velde & Meysman, 2016), as evidenced by our observations. Our results indicate that greigite formation and preservation modulated by turbidites and bioturbation in deep-sea fan sediments could be an overlooked Fe–S sink and that mineral magnetic methods may offer an approach for better understanding of the marine Fe–S–C cycle.

6. Conclusions

Mineral magnetic measurements in combination with SEM/EDS observations, and EPMA and XRD analyses demonstrate the presence of massive coarse-grained (up to ~50–75 μm) greigite confined to multiple horizons that lie immediately below the most bioturbated intervals at the top of muddy turbidite beds in the Sumatra Subduction Margin cored by IODP Expedition 362. These greigite-bearing horizons also have elevated TOC and TN contents than elsewhere in the sediment column. The greigite is associated with successive organic-rich turbidites that have tops reworked by intense bioturbation. This leads to enrichment of organic matter, iron (oxyhydr)oxides, Fe^{2+}, and sulfides and/or sulfate in the intensely bioturbated horizons at the top of turbidite beds, which favors greigite formation and preservation within a closed diagenetic system created by neighboring turbidite beds. This may be a new greigite formation pathway under conditions modulated by turbidites and bioturbation. The formation of abundant coarse-grained greigite results in anomalously high magnetic susceptibility and NRM. Paleomagnetic analyses indicate that these greigite-bearing sediments preserve a quasi-primary paleomagnetic record that was acquired in an early stage after deposition. Early diagenetic greigite may, thus, yield reliable near-syn-sedimentary magnetic signals for paleoenvironmental and paleomagnetic studies. The large greigite concentrations imply that similar intensely bioturbated turbiditic sediments are an important iron and sulfur sink and play an important role in the global Fe–S–C cycle.

Data Availability Statement

All Expedition 362 data used for this study are available in the Zenodo database (https://web.iodp.tamu.edu/publish/01/OVERVIEW.HTML), including (a) downhole magnetic susceptibility measured onboard with the SHMSL instrument (https://doi.org/10.5281/zenodo.3754971), and (b) NRM measured onboard with the 2G three-axis pass-through superconducting rock magnetometer (https://doi.org/10.5281/zenodo.3754797). Other rock magnetic and paleomagnetic data, TOC/TN data, and XRD data collected for this study can be found at: https://doi.org/10.5281/zenodo.7025598.

References

Aben, F. M., Dekkers, M. J., Bakker, R. R., van Hinsbergen, D. J. J., Zachariasse, W. J., Tate, G. W., et al. (2014). Untangling inconsistent magnetic polarity records through an integrated rock magnetic analysis: A case study on Neogene sections in East Timor. *Geochemistry, Geophysics, Geosystems*, *15*, 2531–2554. https://doi.org/10.1002/2014GC005294

Acton, G. D. (1999). Apparent polar wander of India since the Cretaceous with implications for regional tectonics and true polar wander. In T. Radhakrishna & J. D. A. Piper (Eds.), *The Indian subcontinent and Gondwana: A palaeomagnetic and rock magnetic perspective. Memoir Geological Society of India* (Vol. 44, pp. 129–175). Geological Society of India.

Aller, R. C. (1994). Bioturbation and remineralization of sedimentary organic matter: Effects of redox oscillation. *Chemical Geology*, *114*(3–4), 331–345. https://doi.org/10.1016/0009-2541(94)90062-0

Anderson, T. F., & Raiswell, R. (2004). Sources and mechanisms for the enrichment of highly reactive iron in euxinic Black Sea sediments. *American Journal of Science*, *304*, 203–233. https://doi.org/10.2475/ajs.304.3.203

Anschutz, P., Jorissen, F. J., Chaillou, G., Abu-Zied, R., & Fontanier, C. (2002). Recent turbidite deposition in the eastern Atlantic: Early diagenesis and biotic recovery. *Journal of Marine Research*, *60*, 835–854. https://doi.org/10.1357/002224002321505156

Aubourg, C., Pozzi, J.-P., & Kars, M. (2012). Burial, claystones remagnetization and some consequences for magnetostratigraphy. In R. D. Elmore, A. R. Muxworthy, M. M. Aldana, & M. Mena (Eds.), *Remagnetization and chemical alteration of sedimentary rocks, Geological Society Special Publication* (Vol. 371, pp. 181–188). Geological Society. https://doi.org/10.1144/sp371.4

Backman, J., Chen, W., Kachovich, S., Mitchison, F. L., Petronotis, K. E., Yang, T., & Zhao, X. (2019). Data report: Revised age models for IODP Sites U1480 and U1481, expedition 362. In L. C. McNeill, B. Dugan, K. E. Petronotis, & The Expedition 362 Scientists (Eds.), *Sumatra subduction zone. Proceedings of the International Ocean Discovery Program, 362*. International Ocean Discovery Program. https://doi.org/10.14379/iodp.proc.362.202.2019

Badesab, F., Dewangan, P., & Gaikwad, V. (2020). Magnetic mineral diagenesis in a newly discovered active cold seep site in the Bay of Bengal. *Frontiers of Earth Science*, *8*, 592557. https://doi.org/10.3389/feart.2020.592557

Berelson, W. M., Morine, L., Sessions, A., Rollins, N., Fleming, J. C., & Schwalbach, J. (2019). Santa Barbara basin flood layers: Impact on sediment diagenesis. In *Mountains to the abyss: The California borderland as an archive of Southern California geologic evolution. SEPM Society for Sedimentary Geology Special Publication* (Vol. 110, pp. 233–240). SEPM Society for Sedimentary Geology. https://doi.org/10.2110/sepmsp.110.11

Berner, R. A. (1984). Sedimentary pyrite formation: An update. *Geochimica et Cosmochimica Acta*, *48*(4), 605–615. https://doi.org/10.1016/0016-7037(84)90089-9

Blanchet, C. L., Thouveny, N., & Vidal, L. (2009). Formation and preservation of greigite (Fe_3S_4) in sediments from the Santa Barbara basin: Implications for paleoenvironmental changes during the past 35 ka. *Paleoceanography*, *24*, PA2224. https://doi.org/10.1029/2008PA001719

Burdige, D. J. (2006). *Geochemistry of marine sediments*. Princeton University Press.

Burton, E. D., Bush, R. T., Johnston, S. G., Sullivan, L. A., & Keene, A. F. (2011). Sulfur biogeochemical cycling and novel Fe–S mineralization pathways in a tidally re-flooded wetland. *Geochimica et Cosmochimica Acta*, *75*(12), 3434–3451. https://doi.org/10.1016/j.gca.2011.03.020

Canfield, D. E. (2001). Biogeochemistry of sulfur isotopes. *Reviews in Mineralogy and Geochemistry*, *43*, 607–636. https://doi.org/10.2138/gsrmg.43.1.607

Canfield, D. E., & Farquhar, J. (2009). Animal evolution, bioturbation, and the sulfate concentration of the oceans. *Proceedings of the National Academy of Sciences of the United States of America*, *106*, 8123–8127. https://doi.org/10.1073/pnas.0902037106

Canfield, D. E., Raiswell, R., & Bottrell, S. (1992). The reactivity of sedimentary iron minerals toward sulfide. *American Journal of Science*, *292*, 659–683. https://doi.org/10.2475/ajs.292.9.659

Chang, L., Roberts, A. P., Muxworthy, A. R., Tang, Y., Chen, Q., Rowan, C. J., et al. (2007). Magnetic characteristics of synthetic pseudo-single-domain and multi-domain greigite (Fe_3S_4). *Geophysical Research Letters*, *34*, L24304. https://doi.org/10.1029/2007GL032114

Chang, L., Roberts, A. P., Rowan, C. J., Tang, Y., Pruner, P., Chen, Q., & Horng, C. S. (2009). Low-temperature magnetic properties of greigite (Fe_3S_4). *Geochemistry, Geophysics, Geosystems*, *10*, Q01Y04. https://doi.org/10.1029/2008GC002276

Chang, L., Roberts, A. P., Tang, Y., Rainford, B. D., Muxworthy, A. R., & Chen, Q. (2008). Fundamental magnetic parameters from pure synthetic greigite (Fe_3S_4). *Journal of Geophysical Research*, *113*, B06104. https://doi.org/10.1029/2007JB005502

Chang, L., Vasiliev, I., Baak, C., Krijgsman, W., Dekkers, M. J., Roberts, A. P., et al. (2014). Identification and environmental interpretation of diagenetic and biogenic greigite in sediments: A lesson from the Messinian Black Sea. *Geochemistry, Geophysics, Geosystems*, *15*, 3612–3627. https://doi.org/10.1002/2014GC005411

Chen, W.-H., Yan, Y., Clift, P. D., Carter, A., Huang, C.-Y., Pickering, K. T., et al. (2020). Drainage evolution and exhumation history of the eastern Himalaya: Insights from the Nicobar Fan, northeastern Indian Ocean. *Earth and Planetary Science Letters*, *548*, 116472. https://doi.org/10.1016/j.epsl.2020.116472

Chen, Y., Zhang, W., Nian, X., Sun, Q., Ge, C., Hutchinson, S. M., et al. (2021). Greigite as an indicator for salinity and sedimentation rate change: Evidence from the Yangtze River Delta, China. *Journal of Geophysical Research: Solid Earth*, *126*, e2020JB021085. https://doi.org/10.1029/2020JB021085

Claypool, G. (2004). Ventilation of marine sediments indicated by depth profiles of pore water sulfate and $\delta^{34}S$. *The Geochemical Society Special Publications*, *9*, 59–65. https://doi.org/10.1016/s1873-9881(04)80007-5

Crimes, P. T., & Fedonkin, M. A. (1994). Evolution and dispersal of deepsea traces. *PALAIOS*, *9*, 74–83. https://doi.org/10.2307/3515080

Cutter, G. A., & Kluckhohn, R. S. (1999). The cycling of particulate carbon, nitrogen, sulfur, and sulfur species (iron monosulfide, greigite, pyrite, and organic sulfur) in the water columns of Framvaren Fjord and the Black Sea. *Marine Chemistry*, *67*(3–4), 149–160. https://doi.org/10.1016/s0304-4203(99)00056-0

Deflandre, B., Mucci, A., Gagné, J.-P., Guignard, C., & Sundby, B. (2002). Early diagenetic processes in coastal marine sediments disturbed by a catastrophic sedimentation event. *Geochimica et Cosmochimica Acta*, *66*(14), 2547–2558. https://doi.org/10.1016/s0016-7037(02)00861-x

Dekkers, M. J., Passier, H. F., & Schoonen, M. A. A. (2000). Magnetic properties of hydrothermally synthesized greigite (Fe_3S_4)—II. High and low-temperature characteristics. *Geophysical Journal International*, *141*(3), 809–819. https://doi.org/10.1046/j.1365-246x.2000.00129.x

de Lange, G. J. (1986). Early diagenetic reactions in interbedded pelagic and turbiditic sediments in the Nares Abyssal Plain (western North Atlantic): Consequences for the composition of sediment and interstitial water. *Geochimica et Cosmochimica Acta*, *50*(12), 2543–2561. https://doi.org/10.1016/0016-7037(86)90209-7

de Lange, G. J. (1998). Oxic vs. anoxic diagenetic alteration of turbiditic sediments in the Madeira Abyssal Plain, eastern North Atlantic. *Proceedings of the Ocean Drilling Program Scientific Results*, *157*, 573–580. https://doi.org/10.2973/odp.proc.sr.157.143.1998

Dewangan, P., Basavaiah, N., Badesab, F. K., Usapkar, A., Mazumdar, A., Joshi, R., & Ramprasad, T. (2013). Diagenesis of magnetic minerals in a gas hydrate/cold seep environment off the Krishna–Godavari basin, Bay of Bengal. *Marine Geology*, *340*, 57–70. https://doi.org/10.1016/j.margeo.2013.04.016

Dong, J., Zhang, S., Jiang, G., Li, H., & Gao, R. (2013). Greigite from carbonate concretions of the Ediacaran Doushantuo Formation in South China and its environmental implications. *Precambrian Research*, *225*, 77–85. https://doi.org/10.1016/j.precamres.2012.03.010

Droser, M. L., & Bottjer, D. J. (1986). A semiquantitative field classification of ichnofabric. *Journal of Sedimentary Research*, *56*(4), 558–559. https://doi.org/10.1306/212f89c2-2b24-11d7-8648000102c1865d

Duan, Z., Liu, Q., Qin, H., Zhao, X., & Gao, X. (2020). Behavior of greigite-bearing marine sediments during AF and thermal demagnetization and its significance. *Geochemistry, Geophysics, Geosystems*, *21*, e2019GC008635. https://doi.org/10.1029/2019GC008635

Dunlop, D. J., & Özdemir, D. (1997). *Rock magnetism: Fundamentals and frontiers*. Cambridge University Press.

Ebert, Y., Shaar, R., Levy, E. J., Zhao, X., Roberts, A. P., & Stein, M. (2020). Magnetic properties of late Holocene Dead Sea sediments as a monitor of regional hydroclimate. *Geochemistry, Geophysics, Geosystems*, *21*, e2020GC009176. https://doi.org/10.1029/2020GC009176

Ebert, Y., Shaar, R., & Stein, M. (2021). Decadal geomagnetic secular variations from greigite bearing Dead Sea sediments. *Geochemistry, Geophysics, Geosystems*, *22*, e2021GC009665. https://doi.org/10.1029/2021GC009665

Florindo, F., Karner, D. B., Marra, F., Renne, P. R., Roberts, A. P., & Weaver, R. (2007). Radioisotopic age constraints for Glacial Terminations IX and VII from aggradational sections of the Tiber River delta in Rome, Italy. *Earth and Planetary Science Letters*, *256*, 61–80. https://doi.org/10.1016/j.epsl.2007.01.014

Florindo, F., & Sagnotti, L. (1995). Palaeomagnetism and rock magnetism in the upper Pliocene Valle Ricca (Rome, Italy) section. *Geophysical Journal International*, *123*(2), 340–354. https://doi.org/10.1111/j.1365-246x.1995.tb06858.x

Fu, C.-F., Bloemendal, J., Qiang, X.-K., Hill, M. J., & An, Z.-S. (2015). Occurrence of greigite in the Pliocene sediments of Lake Qinghai, China, and its paleoenvironmental and paleomagnetic implications. *Geochemistry, Geophysics, Geosystems*, *16*, 1293–1306. https://doi.org/10.1002/2014GC005677

Fu, Y., von Dobeneck, T., Franke, C., Heslop, D., & Kasten, S. (2008). Rock magnetic identification and geochemical process models of greigite formation in Quaternary marine sediments from the Gulf of Mexico (IODP Hole U1319A). *Earth and Planetary Science Letters*, *275*, 233–245. https://doi.org/10.1016/j.epsl.2008.07.034

Goldstein, J. I., Newbury, D. E., Michael, J. R., Ritchie, N. W. M., Scott, J. H. J., & Joy, D. C. (2017). *Scanning electron microscopy and X-ray microanalysis*. Springer.

Greve, A., Kars, M., & Dekkers, M. J. (2021). Fluid accumulation, migration and anaerobic oxidation of methane along a major splay fault at the Hikurangi subduction margin (New Zealand): A magnetic approach. *Journal of Geophysical Research: Solid Earth*, *126*, e2020JB020671. https://doi.org/10.1029/2020JB020671

Harrison, R. J., & Feinberg, J. M. (2008). FORCinel: An improved algorithm for calculating first-order reversal curve distributions using locally weighted regression smoothing. *Geochemistry, Geophysics, Geosystems*, *9*, Q05016. https://doi.org/10.1029/2008GC001987

Heard, T. G., Pickering, K. T., & Clark, J. D. (2014). Ichnofabric characterization of a deep-marine clastic system: A subsurface study of the middle Eocene Ainsa System, Spanish Pyrenees. *Sedimentology*, *61*(5), 1298–1331. https://doi.org/10.1111/sed.12101

Hirt, A. M., Banin, A., & Gehring, A. U. (1993). Thermal generation of ferromagnetic minerals from iron-enriched smectites. *Geophysical Journal International*, *115*(3), 1161–1168. https://doi.org/10.1111/j.1365-246x.1993.tb01518.x

Hoffmann, V. (1992). Greigite (Fe_3S_4): Magnetic properties and first domain observations. *Physics of the Earth and Planetary Interiors*, *70*, 288–301. https://doi.org/10.1016/0031-9201(92)90195-2

Hoffmann, V., Stanjek, H., & Murad, E. (1993). Mineralogical, magnetic and Mössbauer data of smythite (Fe$_9$S$_{11}$). *Studia Geophysica et Geodaetica*, *37*, 366–381. https://doi.org/10.1007/bf01613583

Horng, C.-S. (2018). Unusual magnetic properties of sedimentary pyrrhotite in methane seepage sediments: Comparison with metamorphic pyrrhotite and sedimentary greigite. *Journal of Geophysical Research: Solid Earth*, *123*, 4601–4617. https://doi.org/10.1002/2017JB015262

Horng, C.-S., Laj, C., Lee, T.-Q., & Chen, J.-C. (1992). Magnetic characteristics of sedimentary rocks from the Tsengwen-chi and Erhjen-chi sections in southwestern Taiwan. *Terrestrial, Atmospheric and Oceanic Sciences*, *3*, 519–532. https://doi.org/10.3319/tao.1992.3.4.519(t)

Horng, C.-S., & Roberts, A. P. (2006). Authigenic or detrital origin of pyrrhotite in sediments?: Resolving a paleomagnetic conundrum. *Earth and Planetary Science Letters*, *241*(3–4), 750–762. https://doi.org/10.1016/j.epsl.2005.11.008

Horng, C.-S., & Roberts, A. P. (2018). The low-temperature Besnus magnetic transition: Signals due to monoclinic and hexagonal pyrrhotite. *Geochemistry, Geophysics, Geosystems*, *19*, 3364–3375. https://doi.org/10.1029/2017GC007394

Horng, C.-S., Roberts, A. P., Chen, Y.-H., Shea, K.-S., Chen, K.-H., Lin, C.-H., et al. (2020). Magnetic properties of sedimentary smythite (Fe$_9$S$_{11}$). *Journal of Geophysical Research: Solid Earth*, *125*, e2019JB018812. https://doi.org/10.1029/2019JB018812

Horng, C.-S., Torii, M., Shea, K.-S., & Kao, S.-J. (1998). Inconsistent magnetic polarities between greigite- and pyrrhotite/magnetite-bearing marine sediments from the Tsailiao-chi section, southwestern Taiwan. *Earth and Planetary Science Letters*, *164*, 467–481. https://doi.org/10.1016/s0012-821x(98)00239-8

House, B. M. (2019). *From the deep earth to the atmosphere: New geochemical approaches to address marine productivity, long-term climate, and continental rifting* (Doctoral dissertation). University of California San Diego. Retrieved from eScholarship https://escholarship.org/uc/item/0xc8n6c0

Housen, B. A., & Musgrave, R. J. (1996). Rock-magnetic signature of gas hydrates in accretionary prism sediments. *Earth and Planetary Science Letters*, *139*(3–4), 509–519. https://doi.org/10.1016/0012-821x(95)00245-8

Hüsing, S. K., Dekkers, M. J., Franke, C., & Krijgsman, W. (2009). The Tortonian reference section at Monte dei Corvi (Italy): Evidence for early remanence acquisition in greigite-bearing sediments. *Geophysical Journal International*, *179*, 125–143.

Jiang, W.-T., Horng, C.-S., Roberts, A. P., & Peacor, D. R. (2001). Contradictory magnetic polarities in sediments and variable timing of neoformation of authigenic greigite. *Earth and Planetary Science Letters*, *193*, 1–12. https://doi.org/10.1016/s0012-821x(01)00497-6

Johnston, S. G., Burton, E. D., Aaso, T., & Tuckerman, G. (2014). Sulfur, iron and carbon cycling following hydrological restoration of acidic freshwater wetlands. *Chemical Geology*, *371*, 9–26. https://doi.org/10.1016/j.chemgeo.2014.02.001

Jørgensen, B. B., Böttcher, M. E., Lüschen, H., Neretin, L. N., & Volkov, I. I. (2004). Anaerobic methane oxidation and a deep H$_2$S sink generate isotopically heavy sulfides in Black Sea sediments. *Geochimica et Cosmochimica Acta*, *68*(9), 2095–2118.

Just, J., & Kontny, A. (2012). Thermally induced alterations of minerals during measurements of the temperature dependence of magnetic susceptibility: A case study from the hydrothermally altered Soultz-sous-Forêts granite, France. *International Journal of Earth Sciences*, *101*, 819–839. https://doi.org/10.1007/s00531-011-0668-9

Just, J., Sagnotti, L., Nowaczyk, N. R., Francke, A., & Wagner, B. (2019). Recordings of fast paleomagnetic reversals in a 1.2 Ma greigite-rich sediment archive from Lake Ohrid, Balkans. *Journal of Geophysical Research: Solid Earth*, *124*, 12445–12464. https://doi.org/10.1029/2019JB018297

Kao, S.-J., Horng, C.-S., Roberts, A. P., & Liu, K.-K. (2004). Carbon–sulfur–iron relationships in sedimentary rocks from southwestern Taiwan: Influence of geochemical environment on greigite and pyrrhotite formation. *Chemical Geology*, *203*, 153–168. https://doi.org/10.1016/j.chemgeo.2003.09.007

Kars, M., Aubourg, C., Labaume, P., Berquó, T. S., & Cavailhes, T. (2014). Burial diagenesis of magnetic minerals: New insights from the Grès D'Annot transect (SE France). *Minerals*, *4*(3), 667–689. https://doi.org/10.3390/min4030667

Kars, M., Aubourg, C., Pozzi, J.-P., & Janots, D. (2012). Continuous production of nanosized magnetite through low grade burial. *Geochemistry, Geophysics, Geosystems*, *13*, Q08Z48. https://doi.org/10.1029/2012GC004104

Kars, M., Greve, A., & Zerbst, L. (2021). Authigenic greigite as an indicator of methane diffusion in gas hydrate-bearing sediments of the Hikurangi Margin, New Zealand. *Frontiers of Earth Science*, *9*, 603363. https://doi.org/10.3389/feart.2021.603363

Kars, M., & Kodama, K. (2015). Authigenesis of magnetic minerals in gas hydrate-bearing sediments in the Nankai Trough, offshore Japan. *Geochemistry, Geophysics, Geosystems*, *16*, 947–961. https://doi.org/10.1002/2014GC005614

Kars, M., Köster, M., Henkel, S., Stein, R., Schubotz, F., Zhao, X., et al. (2021). Influence of early low-temperature and later high-temperature diagenesis on magnetic mineral assemblages in marine sediments from the Nankai Trough. *Geochemistry, Geophysics, Geosystems*, *22*, e2021GC010133. https://doi.org/10.1029/2021GC010133

Kasten, S., Freudenthal, T., Gingele, F. X., & Schulz, H. D. (1998). Simultaneous formation of iron-rich layers at different redox boundaries in sediments of the Amazon deep-sea fan. *Geochimica et Cosmochimica Acta*, *62*(13), 2253–2264. https://doi.org/10.1016/s0016-7037(98)00093-3

Kelder, N. A., Sant, K., Dekkers, M. J., Magyar, I., van Dijk, G. A., Lathouwers, Y. Z., et al. (2018). Paleomagnetism in Lake Pannon: Problems, pitfalls, and progress in using iron sulfides for magnetostratigraphy. *Geochemistry, Geophysics, Geosystems*, *19*, 3405–3429. https://doi.org/10.1029/2018GC007673

Kirschvink, J. L. (1980). The least-squares line and plane and the analysis of palaeomagnetic data. *Geophysical Journal of the Royal Astronomical Society*, *62*(3), 699–718. https://doi.org/10.1111/j.1365-246x.1980.tb02601.x

Kopp, R. E., & Kirschvink, J. L. (2008). The identification and biogeochemical interpretation of fossil magnetotactic bacteria. *Earth-Science Reviews*, *86*(1–4), 42–61. https://doi.org/10.1016/j.earscirev.2007.08.001

Koymans, M. R., van Hinsbergen, D. J. J., Pastor Galán, D., Vaes, B., & Langereis, C. G. (2020). Towards FAIR paleomagnetic data management through Paleomagnetism.org 2.0. *Geochemistry, Geophysics, Geosystems*, *21*, e2019GC008838. https://doi.org/10.1029/2019GC008838

Krs, M., Krsová, M., Pruner, P., Zeman, A., Novák, F., & Jansa, J. (1990). A petromagnetic study of Miocene rocks bearing microorganic material and the magnetic mineral greigite (Sokolov and Cheb basins, Czechoslovakia). *Physics of the Earth and Planetary Interiors*, *63*, 98–112. https://doi.org/10.1016/0031-9201(90)90064-5

Larrasoaña, J. C., Roberts, A. P., Musgrave, R. J., Gràcia, E., Piñero, E., Vega, M., & Martínez-Ruiz, F. (2007). Diagenetic formation of greigite and pyrrhotite in marine sedimentary systems containing gas hydrates. *Earth and Planetary Science Letters*, *261*, 350–366.

Larrasoaña, J. C., Roberts, A. P., Stoner, J. S., Richter, C., & Wehausen, R. (2003). A new proxy for bottom-water ventilation in the eastern Mediterranean based on diagenetically controlled magnetic properties of sapropel-bearing sediments. *Palaeogeography, Palaeoclimatology, Palaeoecology*, *190*, 221–242.

Lascu, I., Einsle, J. F., Ball, M. R., & Harrison, R. J. (2018). The vortex state in geologic materials: A micromagnetic perspective. *Journal of Geophysical Research: Solid Earth*, *123*, 7285–7304. https://doi.org/10.1029/2018JB015909

Lesniak, B., Koulialias, D., Charilaou, M., Weidler, P. G., Rhodes, J. M., Macdonald, J. E., & Gehring, A. U. (2021). Polycrystalline texture causes magnetic instability in greigite. *Scientific Reports*, *11*, 3024. https://doi.org/10.1038/s41598-020-80801-4

Li, G.-W., Zhang, B.-M., Yu, F., Novakova, A. A., Krivenkov, M. S., Kiseleva, T. Y., et al. (2014). High-purity Fe_3S_4 greigite microcrystals for magnetic and electrochemical performance. *Chemistry of Materials*, *26*(20), 5821–5829. https://doi.org/10.1021/cm501493m

Lin, Z.-Y., Sun, X.-M., Roberts, A. P., Strauss, H., Lu, Y., Yang, X., et al. (2021). A novel authigenic magnetite source for sedimentary magnetization. *Geology*, *49*(4), 360–365. https://doi.org/10.1130/g48069.1

Liu, J., Zhu, R.-X., Li, S.-Q., & Chang, J.-H. (2005). Magnetic mineral diagenesis in the post-glacial muddy sediments from the southeastern South Yellow Sea: Response to marine environmental changes. *Science in China – Series D: Earth Sciences*, *48*, 134–144. https://doi.org/10.1360/02yd0302

Liu, J., Zhu, R.-X., Roberts, A. P., Li, S.-Q., & Chang, J.-H. (2004). High-resolution analysis of early diagenetic effects on magnetic minerals in post-Middle-Holocene continental shelf sediments from Korea Strait. *Journal of Geophysical Research*, *109*, B03103. https://doi.org/10.1029/2003JB002813

Liu, J.-B., Nowaczyk, N. R., Frank, U., & Arz, H. W. (2018). A 20–15 ka high-resolution paleomagnetic secular variation record from Black Sea sediments—No evidence for the 'Hilina Pali excursion'? *Earth and Planetary Science Letters*, *492*, 174–185. https://doi.org/10.1016/j.epsl.2018.04.014

Liu, J.-X., Mei, X., Shi, X.-F., Liu, Q.-S., Liu, Y.-G., & Ge, S.-L. (2018). Formation and preservation of greigite (Fe_3S_4) in a thick sediment layer from the central South Yellow Sea. *Geophysical Journal International*, *213*(1), 135–146. https://doi.org/10.1093/gji/ggx556

Liu, J.-X., Shi, X.-F., Ge, S.-L., Liu, Q.-S., Yao, Z.-Q., & Yang, G. (2014). Identification of the thick-layer greigite in sediments of the South Yellow Sea and its geological significances. *Chinese Science Bulletin*, *59*(22), 2764–2775. https://doi.org/10.1007/s11434-014-0166-0

Liu, S.-Z., Krijgsman, W., Dekkers, M. J., & Palcu, D. (2017). Early diagenetic greigite as an indicator of paleosalinity changes in the middle Miocene Paratethys Sea of central Europe. *Geochemistry, Geophysics, Geosystems*, *18*, 2634–2645. https://doi.org/10.1002/2017GC006988

Liu, X., Fike, D., Li, A., Dong, J., Xu, F., Zhuang, G., et al. (2019). Pyrite sulfur isotopes constrained by sedimentation rates: Evidence from sediments on the East China Sea inner shelf since the late Pleistocene. *Chemical Geology*, *505*, 66–75. https://doi.org/10.1016/j.chemgeo.2018.12.014

Lurcock, P. C., & Wilson, G. S. (2012). PuffinPlot: A versatile, user-friendly program for paleomagnetic analysis. *Geochemistry, Geophysics, Geosystems*, *13*, Q06Z45. https://doi.org/10.1029/2012GC004098

McKay, J. L., & Pedersen, T. F. (2014). Geochemical response to pulsed sedimentation: Implications for the use of Mo as a paleo-proxy. *Chemical Geology*, *382*, 83–94. https://doi.org/10.1016/j.chemgeo.2014.05.009

McNeill, L. C., Dugan, B., Backman, J., Pickering, K. T., Pouderoux, H. F. A., Henstock, T. J., et al. (2017). Understanding Himalayan erosion and the significance of the Nicobar Fan. *Earth and Planetary Science Letters*, *475*, 134–142. https://doi.org/10.1016/j.epsl.2017.07.019

McNeill, L. C., Dugan, B., & Petronotis, K. E., & The Expedition 362 Scientists. (2017). Sumatra subduction zone. In *Proceedings of the International Ocean Discovery Program* (Vol. 362). International Ocean Discovery Program.

Mullender, T. A. T., van Velzen, A. J., & Dekkers, M. J. (1993). Continuous drift correction and separate identification of ferrimagnetic and paramagnetic contribution in thermomagnetic runs. *Geophysical Journal International*, *114*(3), 663–672. https://doi.org/10.1111/j.1365-246x.1993.tb06995.x

Murowchick, J. B., & Barnes, H. L. (1987). Effects of temperature and degree of supersaturation on pyrite morphology. *American Mineralogist*, *72*(11–12), 1241–1250.

Musgrave, R. J., Collombat, H., & Didenko, A. N. (1995). Magnetic sulfide diagenesis, thermal overprinting, and paleomagnetism of accretionary wedge and convergent margin sediments from the Chile Triple Junction region. *Proceedings of the Ocean Drilling Program Scientific Results*, *141*, 59–78. https://doi.org/10.2973/odp.proc.sr.141.015.1995

Musgrave, R. J., Kars, M., & Vega, M. E. (2019). Progressive and punctuated magnetic mineral diagenesis: The rock magnetic record of multiple fluid inputs and progressive pyritization in a volcano-bounded basin, IODP Site U1437, Izu rear arc. *Journal of Geophysical Research: Solid Earth*, *124*, 5357–5378. https://doi.org/10.1029/2018JB017277

Neretin, L. N., Böttcher, M. E., Jørgensen, B. B., Volkov, I. I., Lüschen, H., & Hilgenfeldt, K. (2004). Pyritization processes and greigite formation in the advancing sulfidization front in the Upper Pleistocene sediments of the Black Sea. *Geochimica et Cosmochimica Acta*, *68*(9), 2081–2093. https://doi.org/10.1016/s0016-7037(03)00450-2

Nilsson, A., Lee, Y. S., Snowball, I., & Hill, M. (2013). Magnetostratigraphic importance of secondary chemical remanent magnetizations carried by greigite (Fe_3S_4) in Miocene sediments, New Jersey shelf (IODP Expedition 313). *Geosphere*, *9*, 510–520. https://doi.org/10.1130/ges00854.1

Otero, X. L., Huerta-Diaz, M. A., & Macias, F. (2003). Influence of a turbidite deposit on the extent of pyritization of iron, manganese and trace metals in sediments from the Guaymas Basin, Gulf of California (Mexico). *Applied Geochemistry*, *18*(8), 1149–1163. https://doi.org/10.1016/s0883-2927(02)00190-7

Palcu, D. V., Tulbure, M., Bartol, M., Kouwenhoven, T. J., & Krijgsman, W. (2015). The Badenian–Sarmatian Extinction Event in the Carpathian foredeep basin of Romania: Paleogeographic changes in the Paratethys domain. *Global and Planetary Change*, *133*, 346–358. https://doi.org/10.1016/j.gloplacha.2015.08.014

Passier, H. F., & Dekkers, M. J. (2002). Iron oxide formation in the active oxidation front above sapropel S1 in the eastern Mediterranean Sea as derived from low-temperature magnetism. *Geophysical Journal International*, *150*(1), 230–240. https://doi.org/10.1046/j.1365-246x.2002.01704.x

Passier, H. F., & de Lange, G. J. (1998). Sedimentary sulfur and iron chemistry in relation to the formation of Eastern Mediterranean sapropels. *Proceedings of the Ocean Drilling Program Scientific Results*, *160*, 249–259. https://doi.org/10.2973/odp.proc.sr.160.020.1998

Passier, H. F., de Lange, G. J., & Dekkers, M. J. (2001). Magnetic properties and geochemistry of the active oxidation front and the youngest sapropel in the eastern Mediterranean Sea. *Geophysical Journal International*, *145*(3), 604–614. https://doi.org/10.1046/j.0956-540x.2001.01394.x

Paterson, G. A., Zhao, X., Jackson, M., & Heslop, D. (2018). Measuring, processing, and analyzing hysteresis data. *Geochemistry, Geophysics, Geosystems*, *19*, 1925–1945. https://doi.org/10.1029/2018GC007620

Pickering, K. T., Pouderoux, H., McNeill, L. C., Backman, J., Chemale, F., Kutterolf, S., et al. (2020). Sedimentology, stratigraphy and architecture of the Nicobar Fan (Bengal–Nicobar Fan System), Indian Ocean: Results from International Ocean Discovery Program Expedition 362. *Sedimentology*, *67*, 2248–2281. https://doi.org/10.1111/sed.12701

Pike, C. R., Roberts, A. P., & Verosub, K. L. (1999). Characterizing interactions in fine magnetic particle systems using first order reversal curves. *Journal of Applied Physics*, *85*(9), 6660–6667. https://doi.org/10.1063/1.370176

Pósfai, M., Cziner, K., Márton, E., Márton, P., Buseck, P. R., Frankel, R. B., & Bazylinski, D. A. (2001). Crystal-size distributions and possible biogenic origin of Fe sulfides. *European Journal of Mineralogy*, *13*(4), 691–703.

Poulton, S. W., Krom, M. D., & Raiswell, R. (2004). A revised scheme for the reactivity of iron (oxyhydr)oxide minerals towards dissolved sulfide. *Geochimica et Cosmochimica Acta*, *68*(18), 3703–3715. https://doi.org/10.1016/j.gca.2004.03.012

Raiswell, R., & Canfield, D. E. (1996). Rates of reaction between silicate iron and dissolved sulfide in Peru Margin sediments. *Geochimica et Cosmochimica Acta*, *60*, 2777–2787. https://doi.org/10.1016/0016-7037(96)00141-x

Raiswell, R., Newton, R., Bottrell, S. H., Coburn, P. M., Briggs, D. E. G., Bond, D. P. G., & Poulton, S. W. (2008). Turbidite depositional influences on the diagenesis of Beecher's Trilobite Bed and the Hunsrück Slate; Sites of soft tissue pyritization. *American Journal of Science*, *308*, 105–129. https://doi.org/10.2475/02.2008.01

Reinholdsson, M., Snowball, I., Zillén, L., Lenz, C., & Conley, D. J. (2013). Magnetic enhancement of Baltic Sea sapropels by greigite magnetofossils. *Earth and Planetary Science Letters*, *366*, 137–150. https://doi.org/10.1016/j.epsl.2013.01.029

Reynolds, R. L., Rosenbaum, J. G., van Metre, P., Tuttle, M., Callender, E., & Goldin, A. (1999). Greigite (Fe_3S_4) as an indicator of drought—The 1912–1994 sediment magnetic record from White Rock Lake, Dallas, Texas, USA. *Journal of Paleolimnology*, *21*, 193–206. https://doi.org/10.1023/a:1008027815203

Reynolds, R. L., Tuttle, M. L., Rice, C. A., Fishman, N. S., Karachewski, J. A., & Sherman, D. M. (1994). Magnetization and geochemistry of greigite-bearing Cretaceous strata, North Slope basin, Alaska. *American Journal of Science*, *294*(4), 485–528. https://doi.org/10.2475/ajs.294.4.485

Riedinger, N., & Brunner, B. (2014). Data report: Concentration and sulfur isotope composition of iron monosulfide and pyrite from sediments collected during IODP Expedition 316, Nankai Trough, Japan. In *Proceedings of the Integrated Ocean Drilling Program, 314/315–316*. https://doi.org/10.2204/iodp.proc.314315316.223.2014

Roberts, A. P. (1995). Magnetic characteristics of sedimentary greigite (Fe_3S_4). *Earth and Planetary Science Letters*, *134*, 227–236.

Roberts, A. P. (2015). Magnetic mineral diagenesis. *Earth-Science Reviews*, *151*, 1–47. https://doi.org/10.1016/0012-821x(95)00131-u

Roberts, A. P., Almeida, T. P., Church, N. S., Harrison, R. J., Heslop, D., Li, Y., et al. (2017). Resolving the origin of pseudo-single domain magnetic behavior. *Journal of Geophysical Research: Solid Earth*, *122*, 9534–9558. https://doi.org/10.1002/2017JB014860

Roberts, A. P., Chang, L., Rowan, C. J., Horng, C. S., & Florindo, F. (2011). Magnetic properties of sedimentary greigite (Fe_3S_4): An update. *Reviews of Geophysics*, *49*, RG1002. https://doi.org/10.1029/2010RG000336

Roberts, A. P., Florindo, F., Larrasoaña, J. C., O'Regan, M. A., & Zhao, X. (2010). Complex polarity pattern at the (former) Plio-Pleistocene global stratotype section at Vrica (Italy): Remagnetization by magnetic iron sulphides. *Earth and Planetary Science Letters*, *292*, 98–111. https://doi.org/10.1016/j.epsl.2010.01.025

Roberts, A. P., Liu, Q. S., Rowan, C. J., Chang, L., Carvallo, C., Torrent, J., & Horng, C.-S. (2006). Characterization of hematite (α-Fe_2O_3), goethite (α-FeOOH), greigite (Fe_3S_4), and pyrrhotite (Fe_7S_8) using first-order reversal curve diagrams. *Journal of Geophysical Research*, *111*, B12S35. https://doi.org/10.1029/2006JB004715

Roberts, A. P., Pike, C. R., & Verosub, K. L. (2000). First-order reversal curve diagrams: A new tool for characterizing the magnetic properties of natural samples. *Journal of Geophysical Research*, *105*(B12), 28461–28475. https://doi.org/10.1029/2000JB900326

Roberts, A. P., Reynolds, R. L., Verosub, K. L., & Adam, D. P. (1996). Environmental magnetic implications of greigite (Fe_3S_4) formation in a 3 m.y. lake sediment record from Butte Valley, northern California. *Geophysical Research Letters*, *23*(20), 859–2862. https://doi.org/10.1029/96GL02831

Roberts, A. P., Stoner, J. S., & Richter, C. (1999). Diagenetic magnetic enhancement of sapropels from the eastern Mediterranean Sea. *Marine Geology*, *153*, 103–116. https://doi.org/10.1016/s0025-3227(98)00087-5

Roberts, A. P., & Turner, G. M. (1993). Diagenetic formation of ferrimagnetic iron sulphide minerals in rapidly deposited marine sediments, South Island, New Zealand. *Earth and Planetary Science Letters*, *115*, 257–273. https://doi.org/10.1016/0012-821x(93)90226-y

Roberts, A. P., & Weaver, R. (2005). Multiple mechanisms of remagnetization involving sedimentary greigite (Fe_3S_4). *Earth and Planetary Science Letters*, *231*(3), 263–277. https://doi.org/10.1016/j.epsl.2004.11.024

Roberts, A. P., Zhao, X., Harrison, R. J., Heslop, D., Muxworthy, A. R., Rowan, C. J., et al. (2018). Signatures of reductive magnetic mineral diagenesis from unmixing of first-order reversal curves. *Journal of Geophysical Research: Solid Earth*, *123*, 4500–4522. https://doi.org/10.1029/2018JB015706

Robinson, S. G. (2001). Early diagenesis in an organic-rich turbidite and pelagic clay sequence from the Cape Verde Abyssal Plain, NE Atlantic: Magnetic and geochemical signals. *Sedimentary Geology*, *143*(1–2), 91–123. https://doi.org/10.1016/s0037-0738(00)00187-1

Robinson, S. G., & Sahota, J. T. (2000). Rock-magnetic characterization of early, redoxomorphic diagenesis in turbiditic sediments from the Madeira Abyssal Plain. *Sedimentology*, *47*(2), 367–394.

Rowan, C. J., & Roberts, A. P. (2006). Magnetite dissolution, diachronous greigite formation, and secondary magnetizations from pyrite oxidation: Unravelling complex magnetizations in Neogene marine sediments from New Zealand. *Earth and Planetary Science Letters*, *241*, 119–137. https://doi.org/10.1016/j.epsl.2005.10.017

Rowan, C. J., Roberts, A. P., & Broadbent, T. (2009). Reductive diagenesis, magnetite dissolution, greigite growth and paleomagnetic smoothing in marine sediments: A new view. *Earth and Planetary Science Letters*, *277*(1–2), 223–235. https://doi.org/10.1016/j.epsl.2008.10.016

Sagnotti, L., Cascella, A., Ciaranfi, N., Macrì, P., Maiorano, P., Marino, M., & Taddeucci, J. (2010). Rock magnetism and palaeomagnetism of the Montalbano Jonico section (Italy): Evidence for late diagenetic growth of greigite and implications for magnetostratigraphy. *Geophysical Journal International*, *180*, 1049–1066. https://doi.org/10.1111/j.1365-246x.2009.04480.x

Sagnotti, L., & Winkler, A. (1999). Rock magnetism and palaeomagnetism of greigite bearing mudstones in the Italian peninsula. *Earth and Planetary Science Letters*, *165*, 67–80. https://doi.org/10.1016/s0012-821x(98)00248-9

Schimmelmann, A. (2011). The "coffin lid" effect: Flood layers and turbidites in Santa Barbara Basin affect diagenesis of organic matter in underlying varved sediment. In M. R. Besonen (Ed.), *Second Workshop of the PAGES Varves Working Group, Program and Abstracts* (pp. 83–86). Corpus Christi.

Schippers, A., & Jørgensen, B. B. (2002). Biogeochemistry of pyrite and iron sulfide oxidation in marine sediments. *Geochimica et Cosmochimica Acta*, *66*(1), 85–92. https://doi.org/10.1016/s0016-7037(01)00745-1

Shaw, T. J., & Meyers, P. A. (1996). The implications of turbidite-driven redox changes in sediments of the Iberia Abyssal Plain. *Proceedings of the Ocean Drilling Program Scientific Results*, *149*, 301–304. https://doi.org/10.2973/odp.proc.sr.149.238.1996

Snowball, I. F. (1991). Magnetic hysteresis properties of greigite (Fe_3S_4) and a new occurrence in Holocene sediments from Swedish Lappland. *Physics of the Earth and Planetary Interiors*, *68*(1–2), 32–40. https://doi.org/10.1016/0031-9201(91)90004-2

Snowball, I. F. (1997). Gyroremanent magnetization and the magnetic properties of greigite-bearing clays in southern Sweden. *Geophysical Journal International*, *129*(3), 624–636. https://doi.org/10.1111/j.1365-246x.1997.tb04498.x

Stephenson, A. (1980). A gyroremanent magnetisation in anisotropic magnetic material. *Nature*, *284*(5751), 49–51. https://doi.org/10.1038/284049a0

Taillefert, M., Beckler, J. S., Cathalot, C., Michalopoulos, P., Corvaisier, R., Kiriazis, N., et al. (2017). Early diagenesis in the sediments of the Congo deep-sea fan dominated by massive terrigenous deposits: Part II—Iron–sulfur coupling. *Deep Sea Research Part II: Topical Studies in Oceanography*, *142*, 151–166. https://doi.org/10.1016/j.dsr2.2017.06.009

Tauxe, L., Mullender, T. A. T., & Pick, T. (1996). Potbellies, wasp-waists, and superparamagnetism in magnetic hysteresis. *Journal of Geophysical Research*, *101*(B1), 571–583. https://doi.org/10.1029/95JB03041

Teal, L. R., Bulling, M., Parker, E. R., & Solan, M. (2008). Global patterns of bioturbation intensity and mixed depth of marine soft sediments. *Aquatic Biology*, *2*, 207–218. https://doi.org/10.3354/ab00052

Tesi, T., Langone, L., Goñi, M. A., Wheatcroft, R. A., Miserocchi, S., & Bertotti, L. (2012). Early diagenesis of recently deposited organic matter: A 9-yr time-series study of a flood deposit. *Geochimica et Cosmochimica Acta*, *83*, 19–36. https://doi.org/10.1016/j.gca.2011.12.026

Thomson, J., Higgs, N. C., Croudace, I. W., Colley, S., & Hydes, D. J. (1993). Redox zonation of elements at an oxic/post-oxic boundary in deep-sea sediments. *Geochimica et Cosmochimica Acta*, *57*(3), 579–595. https://doi.org/10.1016/0016-7037(93)90369-8

Thomson, J., Jarvis, I., Green, D. R. H., Green, D. A., & Clayton, T. (1998). Mobility and immobility of redox-sensitive elements in deep-sea turbidites during shallow burial. *Geochimica et Cosmochimica Acta*, *62*(4), 643–656. https://doi.org/10.1016/s0016-7037(97)00378-5

Torii, M., Fukuma, K., Horng, C.-S., & Lee, T.-Q. (1996). Magnetic discrimination of pyrrhotite- and greigite-bearing sediment samples. *Geophysical Research Letters*, *23*(14), 1813–1816. https://doi.org/10.1029/96GL01626

Valdez-Grijalva, M. A., Nagy, L., Muxworthy, A. R., Williams, W., & Fabian, K. (2018). The magnetic structure and palaeomagnetic recording fidelity of sub-micron greigite (Fe$_3$S$_4$). *Earth and Planetary Science Letters*, *483*, 76–89. https://doi.org/10.1016/j.epsl.2017.12.015

Van Baak, C. G. C., Vasiliev, I., Palcu, D. V., Dekkers, M. J., & Krijgsman, W. (2016). A greigite-based magnetostratigraphic time frame for the Late Miocene to recent DSDP Leg 42B cores from the Black Sea. *Frontiers of Earth Science*, *4*, 60. https://doi.org/10.3389/feart.2016.00060

vande Velde, S., & Meysman, F. J. R. (2016). The influence of bioturbation on iron and sulphur cycling in marine sediments: A model analysis. *Aquatic Geochemistry*, *22*(5–6), 469–504. https://doi.org/10.1007/s10498-016-9301-7

Vasiliev, I., Dekkers, M. J., Krijgsman, W., Franke, C., Langereis, C. G., & Mullender, T. A. T. (2007). Early diagenetic greigite as a recorder of the palaeomagnetic signal in Miocene–Pliocene sedimentary rocks of the Carpathian foredeep (Romania). *Geophysical Journal International*, *171*(2), 613–629. https://doi.org/10.1111/j.1365-246x.2007.03560.x

Vasiliev, I., Franke, C., Meeldijk, J. D., Dekkers, M. J., Langereis, C. G., & Krijgsman, W. (2008). Putative greigite magnetofossils from the Pliocene epoch. *Nature Geoscience*, *1*(11), 782–786. https://doi.org/10.1038/ngeo335

Volvoikar, S., Mazumdar, A., Peketi, A., Dewangan, P., Sawant, B., Manaskanya, A., et al. (2020). Contrasting sulfidization in the turbidite and hemipelagic sediments of Bengal Fan. *Marine and Petroleum Geology*, *118*, 104408. https://doi.org/10.1016/j.marpetgeo.2020.104408

Wang, Q., & Morse, J. W. (1996). Pyrite formation under conditions approximating those in anoxic sediments I. Pathway and morphology. *Marine Chemistry*, *52*, 99–121. https://doi.org/10.1016/0304-4203(95)00082-8

Wang, Y., Hendy, I. L., Latimer, J. C., & Bilardello, D. (2019). Diagenesis and iron paleo-redox proxies: New perspectives from magnetic and iron speciation analyses in the Santa Barbara Basin. *Chemical Geology*, *519*, 95–109. https://doi.org/10.1016/j.chemgeo.2019.04.018

Watson, J. H. P., Cressey, B. A., Roberts, A. P., Ellwood, D. C., Charnock, J. M., & Soper, A. K. (2000). Structural and magnetic studies on heavy-metal-adsorbing iron sulphide nanoparticles produced by sulphate-reducing bacteria. *Journal of Magnetism and Magnetic Materials*, *214*(1–2), 13–30. https://doi.org/10.1016/s0304-8853(00)00025-1

Weaver, R., Roberts, A. P., & Barker, A. J. (2002). A late diagenetic (synfolding) magnetization carried by pyrrhotite: Implications for paleomagnetic studies from magnetic iron sulphide-bearing sediments. *Earth and Planetary Science Letters*, *200*(3–4), 371–386. https://doi.org/10.1016/s0012-821x(02)00652-0

Wijsman, J. W. M., Middelburg, J. J., & Heip, C. H. R. (2001). Reactive iron in Black Sea sediments: Implications for iron cycling. *Marine Geology*, *172*, 167–180. https://doi.org/10.1016/s0025-3227(00)00122-5

Yang, T., Dekkers, M. J., & Chen, J. (2018). Thermal alteration of pyrite to pyrrhotite during earthquakes: New evidence of seismic slip in the rock record. *Journal of Geophysical Research: Solid Earth*, *123*, 1116–1131. https://doi.org/10.1002/2017JB014973

Yang, T., Zhao, X., Petronotis, K., Dekkers, M. J., & Xu, H. (2019). Anisotropy of magnetic susceptibility (AMS) of sediments from Holes U1480E and U1480H, IODP Expedition 362: Sedimentary or artificial origin and implications for paleomagnetic studies. *Geochemistry, Geophysics, Geosystems*, *20*, 5192–5215. https://doi.org/10.1029/2019GC008721

Yucel, M., Konovalov, S. K., Moore, T. S., Janzen, C. P., & Luther, G. W., III. (2010). Sulfur speciation in the upper Black Sea sediments. *Chemical Geology*, *269*(3–4), 364–375. https://doi.org/10.1016/j.chemgeo.2009.10.010

Yucel, M., Luther, G. W., III, & Moore, W. S. (2010). Earthquake-induced turbidite deposition as a previously unrecognized sink for hydrogen sulfide in the Black Sea sediments. *Marine Chemistry*, *121*(1–4), 176–186. https://doi.org/10.1016/j.marchem.2010.04.006